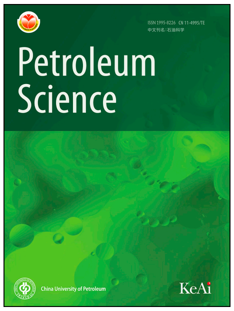

Influencing mechanism of saline sediments on pore system formation and evolution in terrestrial shales

Yuqi Wu, Fujie Jiang, Di Chen, Jing Guo, Chenxi Zhu, Zhao Zhao, Zhuoyue Yan, Tao Hu

PII: S1995-8226(23)00166-8

DOI: https://doi.org/10.1016/j.petsci.2023.06.010

Reference: PETSCI 560

To appear in: *Petroleum Science*

Received Date: 14 October 2022

Revised Date: 11 January 2023

Accepted Date: 29 June 2023

Please cite this article as: Wu, Y., Jiang, F., Chen, D., Guo, J., Zhu, C., Zhao, Z., Yan, Z., Hu, T., Influencing mechanism of saline sediments on pore system formation and evolution in terrestrial shales, *Petroleum Science* (2023), doi: https://doi.org/10.1016/j.petsci.2023.06.010.

Credit authors statement

Chenxi Zhu: Conceptualization, Methodology, Software, Writing–Original draft preparation. Fujie Jiang: Supervision. Pengyuan Zhang: Review & Editing. Zhao Zhao: Validation. Xin Chen: Validation. Yuqi Wu: Data curation. Yuanyuan Chen: Investigation. Wei Wang: Investigation. Zezhang Song: Supervision. Tao Hu: Supervision. Tianwu Xu: Visualization. Yongshui Zhou: Visualization.

Influencing mechanism of saline sediments on pore system formation and evolution in terrestrial shales

Yuqi Wu[a, b]; Fujie Jiang[a, b*]; Di Chen[a, b*]; Jing Guo[a, b]; Chenxi Zhu[a, b]; Zhao Zhao[c]; Zhuoyue Yan[a, b]; Tao Hu[a, b]

[a] State Key Laboratory of Petroleum Resources and Prospecting, China University of Petroleum, Beijing 102249, China;

[b] College of Geosciences, China University of Petroleum, Beijing 102249, China;

[c] Tianjin Branch of CNOOC China Ltd.,Tianjin 300452, China;

* Corresponding address: jfjhtb@163.com (F. Jiang) and cd18801323769@163.com (D. Chen)

Abstract

The majority of oil and gas resources in the world are related to saline sediments, which mainly occur in sedimentary strata in the form of cap rocks or salt-associated shales. A large number of shale oil resources have been discovered in the saline shale sediments of the Cenozoic terrestrial lake basin in China. The hydrocarbon generation ability and the reservoir capacity of shale control the oil and gas generation. The reservoir capacity is mainly characterized by pore type, structure and porosity. Most of China's shale oil and gas resources belong to salt-bearing formations. The role of gypsum-salt rocks in the formation and evolution of organic matter (OM) in such formations has received extensive attention. However, systematic understanding is lacking. Research on the pore formation and evolution in shale under the action of gypsum-salt rock sediments is especially weak. Taking the shales in the third member of the Shahejie Formation (Es_3) of the Bohai Bay Basin as an example, the influence of halite on the formation and evolution process of pores was studied in this paper. The results show that halite and gypsum minerals were associated with OM, which made them more likely to develop OM pores. The samples with a high halite mineral content (HC) are more developed regarding the pore volume and specific surface area than those with a low HC. The formation of thick salt rocks is influenced by factors of deep thermal brine upwelling, sea erosion and arid environments. The frequent alternation between humid and arid environments led to the outbreak and death of organisms and the precipitation of gypsum-salt rock, which formed the simultaneous deposition of OM and halite minerals. Finally, we have established a model of shale pore evolution under the participation of the gypsum-salt rock, and halite minerals contribute to pore development in both Stage II and Stage IV. This study provides strong microscopic evidence for the pore system formation and evolution in salt-bearing reservoirs.

Keywords: Bohai Bay Basin, Dongpu Depression, Pore evolution, Salt-associated shale, Halite mineral

1. Introduction

As an important unconventional oil and gas resource, shale oil and gas have excellent exploration potential (Tang, 1990; Martini et al., 2003; Bowker, 2007; Ross and Bustin, 2008a; Zou et al., 2010; Hu et al., 2022a). By 2019, American shale oil production accounted for 50% of its total crude oil production, achieving energy independence and profoundly impacting on the world energy landscape (Jin et al., 2019). China’s shale oil exploration and development is mainly in a period of industrial testing and exploration breakthroughs (Kuang et al., 2021), with recoverable shale oil reserves estimated at 5×10^9 t (Zou et al., 2020). Shale oil is being developed industrially in the Bohai Bay Basin, Tarim Basin, Ordos Basin, Sichuan Basin, Jianghan Basin and Junggar Basin in China (Jiang et al., 2016, 2018, 2022; Wang et al., 2019, 2020; He et al., 2022). The oil-bearing evaluation method of shale oil is relatively mature (Chen et al., 2021a; Hu et al., 2021c). With the deepening of unconventional oil and gas exploration and development, the shale reservoir microscopic pore space as a shale oil and gas carrier has received increasing attention worldwide. Shale oil and gas are mainly stored in free and adsorbed states in micro-nano pores (Chen et al., 2016; Hu et al., 2021b). The matrix pore space and microfractures constitutes the formation, storage and migration system of shale oil and gas (Xu et al., 2022). Revealing the pore structure characteristics and pore evolution mechanism of shale is significant to the study of shale oil and gas enrichment, reservoir formation and mobility.

According to the International Union of Pure and Applied Chemistry (IUPAC) pore size classification criteria, shale pores are mainly classified as micropores (<2 nm), mesopores (2-50 nm) and macropores (>50 nm) (Chalmers et al., 2012). Low-pressure CO_2 adsorption, low-temperature N_2 adsorption and high-pressure mercury injection enable the quantitative characterization of micropores, mesopores and macropores in shales (Ross and Bustin, 2008b; Sun et al., 2015; Wang et al., 2015). Shale pore types are mainly divided into interparticle pores, intraparticle pores, organic matter (OM) pores and microfractures (Loucks et al., 2009, 2012). Field emission scanning electron microscopy (FE-SEM) allows for the qualitative observation of shale microscopic pore structures and qualitative analysis of pores (Ko et al., 2016; Shao et al., 2019). Scholars have also used nano-computed tomography (nano-CT) and nuclear magnetic resonance (NMR) techniques to study morphology and distribution of OM pores and the pore-throat characteristics of inorganic pores (Jiang et al., 2017, 2019; Chen et al., 2021b). In terms of shale pore evolution, scholars have conducted some research on the evolution of shale pores in natural evolution sections (Mastalerz et al., 2013). These studies have revealed the factors influencing pore evolution by analyzing and testing samples from different well locations and depths. However, the experimental results often contain errors due to differences in the original depositional environment, the geological action experienced and the evolution history of different samples. Thermal simulation experiments can individually control the composition of shale samples, static rock pressure, openness of the system, water content and other factors (Liu and Li, 2020), thereby effectively solving the problem of the heterogeneity of shale samples (He et al., 2018) and enabling the study of the pore evolution process of the same shale sample.

Most of the world’s hydrocarbon resources are associated with saline sediments (Edgell et al., 1996; Ma et al., 2000), mainly hosted in sedimentary strata as cap rocks or associated with shales (Guo et al., 2022). Industrial oil and gas fields have been discovered in 115 salt-bearing basins worldwide, accounting for 89% of the world’s proven oil reserves and 80% of the natural gas reserves (Hudec et al., 2006; Tao et al., 2015). Forty-one percent of these basins are post-salt hydrocarbon resources, and 13% are inter-salt hydrocarbon resources. At present, large quantities of shale oil resources have been found in the saline shale of the Cenozoic terrestrial lacustrine basins in China, and the resources of shale oil in the exploration area in eastern China are greater than 7 billion tons (Li et al., 2021). Many of the world's salt-bearing basins, such as the Bohai Bay Basin, the Jianghan Basin, the Persian Gulf Basin and the Midland Basin, are rich in hydrocarbon resources (Edgell, 1996; Ulisses and Carry, 1996; Jin et al., 2000; Wang et al., 2020), and 58% of hydrocarbon reserves are associated with salt-bearing basins (Peng et al., 2014). China's salt-bearing basins are mainly terrestrial faulted lacustrine basins (Hu et al., 2021a; Zhu et al., 2021), and gypsum-salt rocks are widely developed in lacustrine deposits. Previous studies have focused on the formation of source rocks and OM enrichment mechanisms in saline lacustrine basins (Chen et al., 2020; Wang et al., 2020b; Hu et al., 2021a, 2022b). Studies on the microscopic characteristics of reservoirs have focused more on OM abundance, type, maturity, diagenesis, hydrocarbon generation and the influence of clay minerals on pore development (Jarvie, 2007; Tian et al., 2012; Huang et al., 2016; Jiang et al., 2017; Zhang et al., 2018; Shao et al., 2019), A few studies were conducted on the reservoir characteristics of inter-salt shales (Luo et al., 2013) and found that halite and gypsum minerals have a certain influence on the thermal evolution of OM (Han and Chen, 2015), so there are also differences in OM pore development in saline shales. In general, research on the influence mechanisms of gypsum-salt rocks on pore development is relatively weak. As a typical terrestrial salt lake basin, the Dongpu Depression has a well-developed gypsum-salt formation, and exploration breakthroughs on this depression have been made. Therefore, we choose the Dongpu Depression in the Bohai Bay Basin as the target, focusing on the formation and evolution of the pore under the participation of the gypsum-salt rocks. Our study revealed influencing factors of gypsum-salt minerals on improving the reservoir space of the shale. It is of guiding significance to the exploration and development of shale oil and gas in salt-bearing basins.

2. Geological Setting

The Bohai Bay Basin is a middle Cenozoic rift basin formed by the subduction of the Eurasian and Pacific plates, and is a typical Cenozoic hydrocarbon-rich basin in the eastern part of the East Asian plate (**Fig. 1a**). Under the tectonism, faults are well developed in the Bohai Bay Basin, forming several sedimentary depressions and a large number of hydrocarbon resources. The Dongpu Depression in the southern part of the Linqing Depression in the Bohai Bay Basin contains large quantities of oil and gas resources and a large number of saline sediments developed during the Cenozoic. The Dongpu Depression is bounded on the east by the Lanliao Fault and the Luxi Uplift. On the west by the Chang Yuan, Shijiaji and Songmiao Faults, which gradually transitions toward the Neihuang Uplift, to the south by the Fengqiu North Fault adjacent to the Lankao Uplift and to the north by the Maling Fault, spreading in a NNE direction and covering an area of approximately 5,300 km^2 (Su et al., 2006; Chen et al., 2012; Liu et al., 2014). The tectonic evolution shows a pattern of “east–west zoning and north–south blocking”. According to the developmental characteristics of salt rocks and the thickness of saline sediments, the salt rocks in the Dongpu Depression are divided into saline, brackish and freshwater areas (**Fig. 1c**).

Fig. 1. Geological setting of the Dongpu Depression. (a) Global Eocene (40 Ma) palaeogeography and deep tectonics map (modified from https://deeptimemaps.com/), (b) Overview map of China showing the location of the Bohai Bay Basin and Dongpu Depression, and (c) structure and deposition map of Dongpu Depression (modified from Shao et al., 2018; Zhu et al., 2021; Jiang et al., 2022)

The fill of the Dongpu Depression is mainly Cenozoic strata, with a total thickness of 4,800 m (Yang, 2007). The Paleoproterozoic strata contain source rock formations and reservoirs, which are the dominant reservoir–cover assemblage. The Dongpu Depression is the only depression in the Bohai Bay Basin that contains salt rocks in all formations of the Paleocene Shahejie Formation, with a total of four sets of saline shale formations with the thickness of 950 m (Liu et al., 2014). The research target is located in the Es$_3$, which is further subdivided into three subsections: upper, middle and lower. As a critical exploration formation, the Es_3 is the source rock formation in the region, and many exploratory wells have been drilled to encounter the gypsum-salt rocks (Shi, 2008). It is characterized by “large variations in lithology and thickness”. The lithological composition is surrounded mainly by gypsum-salt rocks, grey and dark mudstone interbedded with siltstone, and grey shale and oil shale (**Fig. 2**).

Fig. 2. Generalized stratigraphy of Dongpu Depression（modified from Zhu et al., 2021; Jiang et al., 2022）

3. Methodology

3.1 Sampling

The experimental samples were selected from four exploratory wells in the saline area of the Dongpu Depression. Nine cores were taken for the low mature saline shale in the upper Es_3. The sampling well locations are shown in **Fig. 1**. We first took 20 g of each sample and divided it into 4 parts of 5 g each. Each part was subjected to *TOC* testing, vitrinite reflectance testing, OM type identification, and XRD analysis to obtain the 4 content, kerogen type, and mineral composition of 9 saline shale samples. Based on the test data, we selected 3 samples with similar burial depths, maturities, 4 contents, kerogen types, and mineral content but different halite mineral content, numbered sample A, B, and C (**Table 1**), and carried out autoclave hydrocarbon generation thermal simulation experiments for the 3 selected samples.

Table 1 Information of shale samples in Dongpu Depression

Sample	Well	Depth, m	Formation	*TOC*, w.t.%	*Ro*, %	Type Index	Kerogen	HC, %
1	PS18-8	3167.5	Es_3^U	1.1738	0.69	57.50	II_1	2.4
2(A)	PS18-8	3168.7	Es_3^U	2.7921	0.73	61.25	II_1	2.8
3	PS18-8	3155.2	Es_3^U	3.2625	0.72	73.50	II_1	1.4
4(B)	PS18-8	3165.8	Es_3^U	1.9123	0.66	67.25	II_1	4.1
5(C)	PS18-8	3156.6	Es_3^U	2.4632	0.63	69.25	II_1	0.9
6	PS18-8	3159.9	Es_3^U	1.5750	0.75	67.00	II_1	6.0
7	Wen15-14	2379.7	Es_3^U	0.4657	0.56	53.50	II_1	1.0

8	Wen10-1	2180.6	Es_3^U	2.8265	0.51	75.25	II_1	1.2
9	Wei18-5	2713.8	Es_3^U	1.2892	0.61	58.00	II_1	0.7

3.2 Methodology

In this study, the autoclave hydrocarbon thermal simulation apparatus was produced by Haian Topsin Research Instruments Co., Ltd. The samples selected were divided into six parts of 50 g each and then cut into 1 cm^3 blocks. According to the “EASY%Ro” model (Sweeney and Burnham, 1990) and type II kerogen thermal simulation experiments in different areas (Chen and Xiao, 2014; Guo et al., 2017; Wang et al., 2022), the experimental temperature and time were set including 4 stages in pore evolution. Five parts of each sample were put into the autoclave hydrocarbon thermal simulation apparatus with a heating rate of 1 ℃/min to 300 ℃, 330 ℃, 360 ℃, 400 ℃ and 500 ℃. The constant temperature was maintained for 24 h to ensure the complete reaction. The remaining original samples were used as calibration samples. After the thermal simulation experiments, XRD analysis, low-pressure CO_2 adsorption, low-temperature N_2 adsorption, high-pressure mercury injection, and SEM experiments were conducted on all samples to characterize the pore size distribution quantitatively and qualitatively observe the pore type and morphology of samples with different halite content (HC) and different thermal evolution degrees. All experiments were completed at the State Key Laboratory of Oil and Gas Resources and Exploration, China University of Petroleum (Beijing).

Low-pressure CO_2 adsorption experiments are suitable for measuring micropores in the range of 0.35-2 nm. Five grams of sample powder (60-80 mesh size) was added to the sample cell for degassing under heating conditions. After degassing, the samples were placed in the analytical device for carbon dioxide adsorption and desorption, and the specific surface area (SSA) and pore volume (PV) were calculated by the Dubinin–Radushkevich (D–R) model (Dubinin and Stoeckli, 1980) and the Dubinin–Astakhov (D–A) model (Dubinin and Stoeckli, 1980).

The low-temperature N_2 adsorption experiments were performed using an instrument manufactured by Quantachrome. Five grams of sample powder (60-80 mesh size) was added to the sample cell and degassed under heating conditions. Then the sample cell was loaded into the analytical device for N_2 adsorption and desorption, and the SSA and PV were calculated by the Brunauer-Emmett-Teller (BET) model and Battet-Joyner-Halenda (BJH) model (Brunauer et al., 1938; Barrett et al., 2002) respectively.

High-pressure mercury injection was applied to measure macropores, and experiments were performed on samples using the Auto Pore IV 9520 instrument. The working temperature of the instrument was 24 ℃ and the working pressures were 0.01 to 430 MPa. The effective pore diameters that could be characterized were 3-120 microns, and the pore radius was obtained by Washburn’s equation (Washburn, 1921).

The relative content of the minerals was calculated by X-ray diffraction analysis. Three grams of sample powder (200-300 mesh size) was used to making a whole rock-thin section and placed in a TTR III multifunctional X-ray diffractometer for the experiment. The mineral content was found by the relationship between the intensity of the characteristic peak of the X-ray diffraction pattern and the mineral content K value.

A biological microscope was used to determine the type of kerogen. The kerogen can be classified as types I, II_1, II_2 and III according to the kerogen sample’s type index (*TI*).

For *TOC* analysis, the sample powder (200 mesh size) was placed in a crucible, diluted hydrochloric acid was added to remove inorganic carbon, and the sample was rinsed with distilled water to a neutral pH value and placed on a LECO CS-230 carbon sulfur analyzer for organic carbon analysis. The SEM allows qualitative observation of pore characteristics. High-quality samples were obtained using the argon ion polishing technique. The polished samples were gold plated and placed on an FEI Quanta 200F SEM (voltage of 15 kV, object distance of 10-12 mm) for observation.

4. Results

4.1 Geochemical characteristics and mineral composition

By geochemical testing and mineral analysis (**Table 1**), the kerogen types of the 9 selected saline shale samples selected were all of type II_1. The vitrinite reflectance (*Ro*) values ranged from 0.51% to 0.75% (average: 0.66%), with a low degree of thermal evolution; the *TOC* contents ranged from 0.47 w.t.% to 3.26 w.t.% (average: 1.97 w.t.%); quartz and feldspar mineral content ranged from 7.2% to 31.1% as tested by XRD analysis (average: 19.8%); carbonate minerals are dominated by calcite, reaching 31.9%; the clay mineral contents were from 19.9% to 50% (average: 30.6%); the HC values were between 0.6% and 6% (average: 2.28%); the gypsum mineral contents were from 0 to 31.6% (average: 6.3%) (**Fig. 3**). The brittleness of the shale is a key indicator that is used to evaluate reservoir compressibility (Xiao et al., 2017). The research introduces the brittleness index (brittleness index = (quartz + calcite + dolomite)/total minerals) to characterize the compressibility (Hu et al., 2021b). Three samples with different HC were selected according to the average value of the halite mineral content, namely sample A (HC=2.8%, brittleness index=0.376), sample B (HC=4.1%, brittleness index=0.573) and sample C (HC=0.9%, brittleness index=0.567) for autoclave hydrocarbon thermal simulation experiments.

Fig. 3. The proportions of mineral composition in the shale sample

4.2 Halite mineral morphology and pore type of the original samples

The role of halite minerals in hydrocarbon generation and capping preservation has been discussed by many scholars (Eyong et al., 2018; Ding et al., 2019; Yan, 2021). However, with the development of shale oil exploration and development in China and the discovery of a large number of saline shales, scholars have started to pay attention to the role of halite minerals in pore evolution (Zuo et al., 2019; Gong, 2020). In fact, most halite minerals have been discovered in marine and terrestrial sedimentary strata. We focused on this issue in our study of the Dongpu Depression. For halite minerals, this paper mainly studies the morphological characteristics of halite minerals and gypsum minerals. In terms of pore types, there are many pore types in the saline shale of the Dongpu Depression. According to the classification of Loucks et al. (2012), the pore types are mainly divided into interparticle pores, intraparticle pores, OM pores and microfractures.

The saline shales of the Es_3^U are widely developed with halite minerals and gypsum minerals. The crystals of the halite minerals are usually cubic and polyhedral (**Fig. 4a, b**). Under dissolution, some halite crystals show round and oval morphologies (**Fig. 4c**) and aggregates are densely massive or sparse salt-sinters (**Fig. 4d, e**), and occasionally large crystal clusters of halite minerals. The halite minerals are mainly developed with interparticle pores and a few intraparticle dissolution pores, which are mainly round, oval and polygonal in shape. Gypsum minerals are strongly affected by dissolution, mainly in the form of tabular, book-page and fine-grained aggregates. Tabular gypsum minerals have more developed intraparticle pores (**Fig. 4f**), mainly round and oval with smaller pore sizes. Book-page gypsum minerals are subject to strong dissolution (**Fig. 4g**), usually forming shrinkage cracks within the minerals. Fine-grained gypsum minerals are mainly filled with quartz and feldspar (**Fig. 4h**), forming interparticle pores between gypsum and mineral particles. The pores produced by the halite minerals themselves can be used as effective pores in shale reservoirs.

Fig. 4. Mineral characteristics of saline and gypsum: (a) Single crystal of halite mineral; (b) Halite minerals distributed in sheets; (c) Round and oval halite minerals; (d) The halite mineral aggregate is dense and massive; (e) sparse salt-sinter halite mineral; (f) Tabular gypsum minerals with intraparticle pores; (g) Book-page gypsum minerals; (h) Fine-grained gypsum minerals with quartz

Interparticle pores are formed by the particles supporting each other in the compaction process. These pores with good connectivity can form a better pore network. The interparticle pores of saline shale in the Es_3^U are more developed and mainly exist at the contact edges of mineral grains with irregular polygonal shapes, such as the interparticle pores of quartz and feldspar (**Fig. 5a, c**), quartz and clay minerals (**Fig. 5b**), clay minerals (**Fig. 5d**), and pyrite and clay minerals (**Fig. 5e**). The size of the interparticle pores varies significantly, usually 30 nm-2 μm.

Fig. 5. Morphological characteristics of interparticle pores: (a) Interparticle pores of quartz and clay; (b) Interparticle pores of clay; (c) Interparticle pores of feldspar; (d) Interparticle pores of clay; (e) Interparticle pores of pyrite and clay

The intraparticle pores are mainly developed as dissolution pores within and at the edges of mineral grains (quartz, feldspar, and dolomite) (**Fig. 6a, b, c**), pyrite interparticle pores (**Fig. 6d**) and pyrite intraparticle pores (**Fig. 6e**). The interparticle pores of framboidal pyrite are irregularly polygonal. In contrast, the dissolved pores of mineral particles are mostly round or oval. Shale can produce a large amount of organic acids during hydrocarbon generation, which can dissolve calcite or dolomite minerals, thus forming secondary pores (Shao et al., 2019). These pores have small pore sizes, generally nanoscale pores.

Fig. 6. Morphological characteristics of intraparticle pores: (a) Intraparticle pores of quartz; (b) Intraparticle pores of feldspar; (c) Intraparticle pores of calcite; (d) Intraparticle pores and interparticle pores of pyrite; (e) Intraparticle pores of pyrite

When the OM reaches a certain thermal evolution degree, the amount of hydrocarbon generation will gradually increase, and the generation and expulsion of hydrocarbons will produce pores inside the OM, thereby forming OM pores (Huang et al., 2013; Lu et al., 2016; Jiang et al., 2017; Debanjan et al., 2021; Zou et al., 2022). The maturity of the shale in the Es_3^U is low, and the OM pores are less developed. There are two types of OM formation in the saline shale. The first type is halite minerals formed around OM (**Fig. 7a, b, c**). The energy spectrum shows medium–high OM content. OM and halite minerals exist in an associated relationship, and a few OM pores are formed in this type of OM. OM associated with halite–gypsum minerals is sedimentary OM. This type of OM is usually deposited simultaneously with halite and gypsum minerals. This phenomenon is widespread in the Es_3^U, where OM shrinkage pores started to develop at the low-maturity stage. The second type is OM formed in the interparticle pores of quartz and feldspar minerals (**Fig. 7d, f**) or formed in the interparticle pores of clay minerals (**Fig. 7e**) with a high OM content and the development of a small number of OM pores, and shrinkage pores are generated around the OM. This type of OM is generally migrating OM. The pore space of brittle minerals and clay minerals is occupied by this type of OM. The interior of migrating OM also contains OM pores.

Fig. 7. Morphological characteristics of OM and OM pores: (a) Round and oval halite minerals associated with organic matter; (b) and (c) Gypsum minerals associated with OM and the occurrence of OM pores; (d) OM formed in the interparticle pores of quartz minerals; (e) OM formed in the interparticle pores of clay; (f) OM formed in the interparticle pores of feldspar minerals

Microfractures are also an important reservoir space in shale reservoirs. Microfractures have large pore diameters and long extensions and can form a pore–fracture linkage system when connected to pores. Some natural cracks play a significant role in the migration and accumulation of hydrocarbons in shale reservoirs (Loucks et al., 2012). Brittle minerals are well developed in the saline shale of the Es_3^U in the Dongpu Depression. Natural microfractures are formed under compaction within brittle minerals, such as quartz (**Fig. 8a**) and feldspar (**Fig. 8b**). During diagenesis, clay minerals can form shrinkage cracks with brittle minerals due to dehydration (**Fig. 8c**).

Fig. 8. Morphological characteristics of cracks: (a) The Crack of quartz minerals under compaction; (b) The Crack of feldspar minerals; (c) The shrinkage cracks of clay minerals

4.3 Pore structure characteristics during thermal simulation

According to the classification of Brunauer (1938), the CO_2 adsorption curve of the saline shale in the Es_3^U is the type I (**Fig. 9**). The CO_2 molecules are adsorbed through the “micropore filling” mechanism, indicating that micropores are widely developed. The adsorption capacity reaches a maximum at 500 °C. N_2 adsorption and desorption curves (**Fig. 10**) show that H_3-type hysteresis are present in the three samples, indicating that slit holes are formed by plate or parallel particles with good pore connectivity. When $p/p_0=0.45$, the desorption curve shows a rapid and large decrease, indicating the existence of a fine neck or ink bottle shaped mesopore. High-pressure mercury injection experiments were used to characterize the pore structure characteristics of the macropores. The mercury injection curves of the three samples showed three different forms (**Fig. 11**). **Fig. 11a** and **Fig. 11b** show that the pore structure of the sample is mainly controlled by macropores. **Fig. 11c** shows that the pore structure of the sample is controlled by both mesopores and macropores.

Fig. 9. CO_2 adsorption curves of three samples: (a) CO_2 adsorption curves of sample A; (b) CO_2 adsorption curves of sample B; (c) CO_2 adsorption curves of sample C

Fig. 10. N_2 adsorption and desorption curves for 3 samples: (a) N_2 adsorption and desorption curves of sample A; (b) N_2 adsorption and desorption curves of sample B; (c) N_2 adsorption and desorption curves of sample C

Fig. 11. High-pressure mercury injection curves of 3 samples: (a) High-pressure mercury injection curves of sample A; (b) High-pressure mercury injection curves of sample B; (c) High-pressure mercury injection curves of sample C

It is clear that for the original samples and at T=300 ℃, the pore size distribution of all pores is similar for 3 samples (**Fig. 12a, b**). However, the frequency of large-aperture pores is significantly higher for samples A and B than for sample C as temperatures rise, indicating that mesopores and macropore obviously control the pore structure of samples A and B, while sample C is mainly controlled by micropores and mesopores (**Fig. 12c, d**). When the thermal simulation temperature reaches 400 ℃ and 500 ℃, the frequency of sample A with pore widths exceeding 100 nm increases obviously. The pore width of sample B is mainly distributed from 10-100 nm, while that of sample C is mainly distributed from 1-50 nm. **Table 2** and **Table 3** show that sample B has a higher average PV for micropores and mesopores, and the average SSA of all types of pores in sample A is higher than that of the other samples, while sample C has the lowest average PV and SSA, indicating that the halite minerals have a positive influence on the pore structure and pore development.

Fig. 12. Pore size distribution of 3 samples at different temperatures: (a) Pore size distribution of original samples; (b) Pore size distribution of samples at 300 ℃; (c) Pore size distribution of samples at 330 ℃; (d) Pore size distribution of samples at 360 ℃; (e) Pore size distribution of samples at 400 ℃; (f) Pore size distribution of samples at 500 ℃

Table 2 The variation feature of the Pore Volume of 3 shale samples during the thermal simulation experiment.

Thermal simulation temperature, ℃		EASY% Ro, %	Pore Volume, cm^3/g				The proportions of pore volume, %		
			Micropore	Mesopore	Macropore	Total pore	Micropore	Mesopore	Macropore
Sample A	Original	0.73	0.00413	0.03056	0.00860	0.04330	10	71	20
	300	0.84	0.00394	0.02979	0.01752	0.05124	8	58	34
	330	0.96	0.00553	0.03520	0.00533	0.04606	12	76	12
	360	1.10	0.00403	0.03315	0.01020	0.04738	8	70	22
	400	1.57	0.00442	0.02957	0.04370	0.07769	6	38	56
	500	2.87	0.00664	0.04144	0.05472	0.10280	6	40	53
	Average		0.00478	0.03329	0.02334	0.06141	8	59	33
Sample B	Original	0.72	0.00578	0.03858	0.00533	0.04969	12	78	11
	300	0.84	0.00562	0.04381	0.00420	0.05364	10	82	8
	330	0.96	0.00327	0.02195	0.03582	0.06105	5	36	59
	360	1.10	0.00548	0.04076	0.05309	0.09932	6	41	53
	400	1.57	0.00440	0.02412	0.02832	0.05684	8	42	50
	500	2.87	0.00674	0.04750	0.08627	0.14051	5	34	61
	Average		0.00521	0.03612	0.03551	0.07684	8	52	40
Sample C	Original	0.72	0.00475	0.02612	0.00269	0.03356	14	78	8
	300	0.84	0.00422	0.02452	0.00321	0.03194	13	77	10
	330	0.96	0.00398	0.02379	0.00311	0.03089	17	70	13
	360	1.10	0.00420	0.03576	0.01031	0.05026	8	71	21
	400	1.57	0.00477	0.01406	0.00683	0.02566	19	55	27
	500	2.87	0.00608	0.03530	0.01471	0.05609	11	63	26
	Average		0.00467	0.02540	0.00681	0.03687	14	69	17

Table 3 The variation feature of surface area of 3 shale samples during the thermal simulation experiment

Thermal simulation Temperature, ℃		EASY% Ro, %	Surface Area, cm^2/g				The proportions of surface area, %		
			Micropore	Mesopore	Macropore	Total pore	Micropore	Mesopore	Macropore
Sample A	Original	0.73	9.58948	7.66540	0.80560	18.06048	53	42	4
	300	0.84	6.89901	7.70970	1.24050	15.84921	44	49	8
	330	0.96	8.03456	9.55440	1.61590	19.20486	42	50	8
	360	1.10	5.32922	7.14570	1.65120	14.12612	38	51	12
	400	1.57	6.74262	4.98422	1.36430	13.09114	52	38	10
	500	2.87	9.44719	9.97950	1.96050	21.38719	44	47	9
	Average		7.67368	7.83982	1.43967	16.95317	45	46	8
Sample B	Original	0.72	9.83658	8.08030	1.00520	18.92208	52	43	5
	300	0.84	10.40398	7.95080	1.30750	19.66228	53	40	7
	330	0.96	2.35622	3.42348	1.30990	7.089600	33	48	18
	360	1.10	6.75952	7.28690	1.08960	15.13602	45	48	7
	400	1.57	4.41178	3.50134	1.07970	8.992820	49	39	12
	500	2.87	10.48896	4.44319	2.40450	17.33665	61	26	14

	Average		7.37617	5.78100	1.36607	14.52324	51	40	9
Sample C	Original	0.72	3.74597	6.62760	0.63140	11.00497	34	60	6
	300	0.84	6.32353	5.11646	0.63930	12.07929	52	42	5
	330	0.96	4.55393	1.72518	0.73230	7.011410	65	25	10
	360	1.10	3.23988	6.20214	1.20120	10.64322	30	58	11
	400	1.57	5.70082	2.28760	1.12730	9.115720	63	25	12
	500	2.87	7.15301	7.23360	1.59300	15.97961	45	45	10
	Average		5.11952	4.86543	0.98742	10.97237	47	44	9

By comparing the PV (**Fig. 13**) and SSA (**Fig. 14**) of the 3 samples, it is clear that the PV of 3 samples shows a tendency of first decrease and then increase. The SSA of the micropores shows a tendency of decreasing, with the PV and SSA of the samples with high HC being higher than those of the samples with low HC (Sample B>Sample A>Sample C). For the PV of the mesopores, three samples generally show a tendency to increase, then decrease and finally increase, with differences between the samples with different halite mineral contents at different stages of evolution. Both sample C (HC=0.9%) and sample A (HC=2.8%) show a tendency to decrease and then increase in PV at the low mature stage. The PV of sample B (HC=4.1%) shows evolutions of increasing and decreasing twice. The SSA of samples C and A shows an evolution of decreasing and increasing, while sample B shows tendencies of increasing and decreasing twice. The PV and SSA of samples B and A are higher than sample C in the mature stage. The PV of macropores shows a stepwise increase throughout the thermal evolution stage, with smaller PV in the mature stage and stable changes in PV in the overmature stage. The SSA shows an overall tendency to decrease and then increase, with more frequent changes in the SSA in the maturity stage. The PV and SSA of the macropores of sample C (the lowest HC) in the overmature stage are lower than those of the other samples.

The total PV (**Fig. 13d**) shows a stepwise increase, while the total SSA (**Fig. 14d**) shows a decreasing and then increasing trend. Micropores contribute the least to the PV, while mesopores and macropores contribute more to the PV. Sample C has a predominant proportion of mesopore PV and a lower proportion of macropore PV while sample B has the closest proportion of mesopores and macropores with the largest total PV; micropores and mesopores contribute the most to the SSA, and macropores contribute the least; sample B has the largest SSA contributed by micropores. The micropores contribute most of the SSA, while the mesopores and macropores provide most of the PV. **Fig. 4** and **Fig. 7** reveal that different pore types exist within the halite minerals themselves and in their surroundings, indicating that the halite minerals play a significant role in the development of pores.

Fig. 13. All types of pore volumes changes of 3 samples vs. EASY%Ro: (a) Micropore volumes of 3samples; (b) Mesopore volumes of 3 samples; (c) Macropore volumes of 3 samples; (d) Total pore volumes of 3 samples

Fig. 14. All types of specific surface areas changes of 3 samples vs. EASY%Ro: (a) Micropore surface areas of 3samples; (b) Mesopore surface areas of 3samples; (c) Macropore surface areas of 3samples; (d) Total pore surface areas of 3samples

4.4 Relationship between the *TOC* conversion rate and pore structure

The *TOC* conversion rate (*TOC* conversion = (original *TOC* content-residual *TOC* content)/original *TOC* content) has been used previously to express the efficiency of organic matter to hydrocarbon conversion (Shen et al., 2001; Wang, 2020). In this study, we calculated the *TOC* conversion rates of 3 samples at each temperature (**Table 4**) and established the relationship between *TOC* conversion rates and the pore structure (**Fig. 15**). Sample B with high HC has a higher *TOC* conversion rate during the thermal evolution. Various pore structure parameters are positively correlated with the *TOC* conversion rate. The results show that the presence of halite minerals significantly influences on the conversion of OM and the development of pores. In the ‘Discussion’ section, we provide a specific analysis of this phenomenon.

Fig. 15. PV and SSA changes of 3 samples vs. Conversion rate of *TOC*: (a) Micropore volumes; (b) Micropore surface areas; (c) Mesopore volumes; (d) Mesopore surface areas; (e) Macropore volumes; (f) Macropore surface areas; (g) Total pore volumes; (h) Total pore surface areas

Table 4 *TOC* content and *TOC* conversion of 3 samples at different temperatures

Sample	HC, %	T, °C	*TOC*, w.t.%	Conversion rate of *TOC*, %
A	2.8	300	1.9668	29.56
		330	1.8779	32.74
		360	1.9162	31.37

		400	1.7215	38.34
		500	1.4787	47.04
B	4.1	300	1.4410	24.65
		330	1.3780	27.94
		360	1.3300	30.45
		400	1.3310	30.40
		500	0.8801	53.98
C	0.9	300	2.0880	15.23
		330	1.8410	25.26
		360	1.6020	34.96
		400	1.5710	36.22
		500	1.4350	41.74

5. Discussion

5.1 Occurrence, factors and implication of halite minerals in organic matter enrichment

Evaporite minerals are widely developed in salt-bearing basins around the globe (Rosa et al., 1992; Li et al., 2014; Xiong et al., 2021). Previous studies have focused on OM enrichment mechanisms and salt rocks on the macroscale, while studies on the microscale are especially weak (Guo and Li, 2022; Wang et al., 2022). In this study, we focus on the characteristics and formation of salt rocks and the implication of salt rocks for OM enrichment.

There are two main sedimentary models of salt rock at the macroscale: giant thick-layered salt rock deposition and thin interbedded salt rock and shale. The first deposition model usually shows a patchy distribution of halite minerals under SEM (**Fig. 4b, d**), which is stable because of crystallization. Salt rocks developed in a period of intense tectonic activity in the basin, and the salt rocks formed by such deposition are usually compact. The primary material source is derived from deep thermal brine activity (Jin and Huang, 1985; Jiang et al., 2022). The intensification of thermal brine activity will cause an increase in lake basin sedimentation, forming a thicker salt rock layer (Chen et al., 2000; Ji et al., 2005). Some scholars also believe that the material source of salt rocks is related to sea erosion. Dinoflagellates, coccoliths, calcareous nannofossils and saline water ichthyolites indicate that the Bohai Bay Basin was influenced by sea erosion during stratigraphic deposition (Gao et al., 2009; Triine et al., 2022; Ahmed et al., 2022). In addition, periods of climatic drought, where the injection of atmospheric precipitation gradually decreases (Schneider et al., 2019) and lake shrinkage makes it easier for salt to reach the separating point, are capable of precipitating large amounts of halite in a short time and forming thick layers of salt rocks.

The second deposition model is characterized by a significant association of OM with halite minerals (**Fig. 7a, b, c**), with halite minerals regularly occurring around the OM. This phenomenon is mainly explained by the “deep-water evaporite deposits” and the frequent fluctuations in the lake level. The “deep-water evaporite deposits” theory suggests that halite is formed under certain water depth conditions and that layered brine is the primary form of salt formation. The “shallow-water evaporite deposits” theory suggests that halite results from continuous evaporation and concentration in lakes. In our study, we support the “deep-water evaporite deposits” theory. The uppermost layer of the lake is the dilution layer, the middle is the halocline, and the lower is the brine layer (Gao et al., 2009; Li et al., 2021). Deep thermal brine not only provides the material source for salt rock formation but also provides the nutrients necessary for biological growth (Li et al., 2018; Zheng et al., 2022), which promotes the proliferation of halophilic organisms in the halocline and provides an abundant supply of OM for the formation of hydrocarbons. At the same time, frequent fluctuations in the lake level lead to the interbedding of shale and salt rock (**Fig. 16**) (Guo, 2018; Mahmoud et al., 2020). Intermittent warm and humid climates occur in an overall dry climate, where freshwater injection leads to a short biological explosion, followed by a climate shift to drought, evaporation of lake water, and sequential death of salt-tolerant and halophilic organisms. A large amount of OM is deposited in a relatively short time. Due to the high salinity of the water body in the lake basin, OM is deposited simultaneously with the precipitated halite minerals. The trace element contents in salt rocks also confirmed the simultaneous deposition of OM and salt rocks. The enrichment of elements such as V, Ni, Sb and Gb shows the existence of more OM in salt rocks (**Fig. 17**). Huang et al. (1989) found yellow fluorescent material in primary inclusions in salt rock samples as amorphous sapropelic kerogen, which also indicate the simultaneous deposition of OM and halite minerals. This layering of brine precipitated salt and stratification was eventually broken up, resulting in alternating halite and shale deposits (Gao et al., 2015; Waele et al., 2020). This research explains this phenomenon from the microscale and provides necessary microscopic evidence for the simultaneous deposition of OM and salt rocks.

Fig. 16. The depositional model of Dongpu Depression for the formation of interbedded halite and shales: (a) Shale deposition during periods of high lake levels; (b) Halite deposition during periods of climatic drought. (c) The model of shale and halite (Modified from Wang et al., 2020a; Li et al., 2021)

Fig. 17. Cross-plots of trace elements to indicate organic matter richness in halite. (a) Ni/Rb vs. V/Rb; (b) Sb/Rb vs. Gd/Rb (Modified from Li et al., 2021)

Experimental studies showed that the pores of samples with high HC are more developed. This phenomenon is mainly caused by the difference in petrologen and the own characteristics of halite minerals. The different depositional environments in which the samples with different halite mineral contents were deposited led to differences in their petrologens. Scholars have conducted hydrocarbon generation thermal simulation experiments on shales of different types of kerogen in the Dongpu Depression and found that type II kerogen samples showed a "bimodal hydrocarbon generation" mode in the mature stage (Zhang and Xu, 2019; Li et al., 2020; Liu et al., 2021). The petrologens of these samples are mainly hydrocarbon-forming organisms of dinoflagellates and coccoliths, which are halophilic (Wang, 2022; Souza et al., 2022). The hydrocarbon generation model may be responsible for the frequent changes in PV and SSA during thermal evolution. However, since the samples after the thermal simulation experiments were not subjected to extraction experiments, this conjecture still needs further experimental evidence. Regarding the influence of halite minerals, previous studies have mainly focused on the macroscale, suggesting that sedimentary rocks in highly saline environments have high OM conversion rates (Du, 2008) and that halite minerals facilitate the hydrocarbon conversion of OM. In this study, the promotion of hydrocarbon transformation of OM occurs mainly in OM associated with halite minerals (**Fig. 18a, b, c**), and the associated halite minerals can better concentrate the heat flow by attaching around the OM, thus accelerating the thermal evolution process and promoting the development of OM pores. The mechanism is the fundamental reason for the promotion of the hydrocarbon transformation of OM.

Fig. 18. OM associated with halite minerals and OM pores under SEM: (a) and (b) OM associated with halite minerals developed more OM pores than OM without halite minerals; (c) Microscopic features in the in backscattering mode

5.2 The role of halite in pore evolution

The mineral composition influences pore evolution, OM hydrocarbon generation and diagenesis, reflecting the joint interaction of OM and inorganic minerals (Wu et al., 2019; Xu et al., 2021). In this study, we focus on the role of halite minerals on pore evolution through the thermal simulation experiments of 3 samples with different halite mineral contents. The content of halite minerals has different effects on the evolution of the pore structure of shales at different temperatures.

5.2.1 Effect of halite minerals on inorganic pores

Through experiments, we found that the micropores and mesopores of the samples exhibit frequent changes during the mature stage due to the combined effect of infilling by liquid hydrocarbons (Loucks and Reed, 2014; Reed, 2020) and dissolution by organic acids (Baruch, 2015; Luo et al., 2017). The hydrocarbon generation of OM produces liquid petroleum and bitumen (Mastalerz et al., 2018; Debanjan et al., 2021), which occupy the pore space. The pyrolysis of kerogen also produces organic acids, whose dissolution can promote the development of mesopores and macropores and the formation of secondary pores (Xu et al., 2021; Cao et al., 2022).

In this process, halite minerals play a positive role. As brittle minerals, halite minerals can produce interparticle and intraparticle pores, providing reservoir space for liquid petroleum and bitumen generated by the pyrolysis of kerogen during hydrocarbon generation, thereby determining the PV and SSA of samples with high HC (**Table 2, Table 3**). During the oil window stage, the hydrocarbon generation and expulsion of the shale will reach a dynamic balance. The presence of halite minerals can improve the connectivity of the shale pores and provide migration channels for the generated hydrocarbons (Ma et al., 2012; Shao et al., 2018). Hydrocarbon generation and expulsion result in frequent increasing and decreasing trends of PV during the evolution of the micropores and mesopores (**Fig. 13a, b, Fig. 14a, b**). In this stage, the hydrocarbon generation environment of kerogen is in a high temperature and pressure stage. High temperatures can melt halite minerals and promote the development of macropores. Therefore, the relative proportion of macropores increases while the proportion of micropores and mesopores decreases. Organic acids and water are produced during the hydrocarbon generation process of OM, which can effect dissolution on halite minerals, enabling them to produce more interparticle and intraparticle pores. Therefore, a high HC sample has a higher micropore and mesopore PV (**Fig. 13a, b**) and SSA (**Fig. 14a, b**) than the other samples.

5.2.2 Effect of halite minerals on organic matter pores

OM pores are generated in the mature stage. The micropore PV and SSA variation is mainly controlled by OM pores (Gu et al., 2021). The OM pore space increases with Ro and is the most developed at the high maturity stage (Ma et al., 2013). Halite minerals have high thermal conductivity and catalyse kerogen hydrocarbon generation. Halite minerals can accelerate the reaction rate of and the generation of oil and gas to improve the production rate and promote the thermal evolution process and the development of OM pores. This property of halite minerals is also illustrated by the high *TOC* conversion of high HC samples (**Table 4**). Hydrocarbons generated in the mature and highly mature stages raise the pore pressure (Liu et al., 2015; Liang et al., 2016; Tenger et al., 2021). The overpressure of the pore system also plays a constructive role in preserving OM pores. Thus, halite minerals play a crucial role in promoting the development and preservation of OM pores.

5.2.3 Influence of salt rocks influencing on pore evolution

Different factors of salt rocks also play different roles in pore evolution. Sample C is the shale under a large thick layer of salt rock with a low HC (**Fig. 4b, d**). Samples A and B are shales in which OM is associated with halite minerals (**Fig. 4a, c**). The thick layer of salt rock has a good sealing effect, which causes the formation of abnormal pressure in the shale layer. The abnormal pressure phenomenon plays a buffering and delaying role in the hydrocarbon generation process leading to the compression of the pore space, which is the inhibiting effect of salt rock on the evolution of shales. The associated halite minerals play an opposite role to that of the thick-layered salt rocks, which contribute to the thermal evolution process and hydrocarbon conversion, resulting in more developed PV and SSA in samples A and B than in sample C.

5.3 Shale pore evolution model under the participation of gypsum-salt rocks

According to the characteristics of saline shale pore evolution under the participation of gypsum-salt rock and its influencing factors, we established a pore evolution model from the mature stage to the over-mature stage (**Fig. 19**). We analyzed the changes of PV and SSA during the pore evolution in the presence of halite minerals.

Fig. 19. Shale pore evolution model under the participation of gypsum-salt rocks

For stage I (*Ro*<0.5%), this stage did not warrant a specific study on the variation in PV and SSA in the immature stage because of the limitation of the sample maturity. Previous studies have been performed on shale samples under natural evolution conditions, and the rapid decrease in PV and SSA at this stage is mainly due to the influence of mechanical compaction (Kuila and Prasad, 2013; Ma et al., 2017; Wang and Guo, 2019; Xu et al., 2021). With increasing burial depth, compaction is enhanced, resulting in a rapid reduction in PV and SSA.

In stage II (*Ro*=0.5%~1.2%), hydrocarbon generation and halite minerals are the main factors controlling PV and SSA. Hydrocarbon generation can promote the development of OM pores, and the organic acids can promote the development of inorganic pores; however, the hydrocarbon generation leads to the liquid petroleum and bitumen generated by the pyrolysis of kerogen occupying the pore space. The presence of halite minerals is the main reason for the frequent changes in PV and SSA at this stage. As catalysts for the pyrolysis of kerogen, halite minerals can promote the production of liquid hydrocarbons. OM associated with halite minerals is more likely to produce OM pores under SEM (**Fig. 20a**). Meanwhile, the interparticle and intraparticle pores of the halite minerals allow the generated liquid hydrocarbons to discharge rapidly, which is the main reason for the frequent changes in PV and SSA. In addition, sample B with a high HC has already undergone mesopore to macropore conversion. In contrast, the volume of macropore pores in samples A and C slowly increased, indicating that halite minerals can cause pore transformation to occur in advance, causing the macropores to dominate, which is conducive to the adjustment and development of reservoir space.

In stage III (*Ro*=1.2%~1.6%), the main factors controlling PV and SSA changes in this stage are pore pressure and the brittle mineral content. Previous studies have shown that specific pressures can promote the thermal evolution process of OM, but too much pressure will inhibit the thermal evolution process instead (Hao et al., 2003; He et al., 2018). Since the autoclave thermal simulation experiments were conducted under a closed system, the cracking of kerogen, liquid hydrocarbons and bitumen will produce gaseous hydrocarbons when entering the high maturity stage, resulting in excessive pore pressure. In the closed system, when the brittleness index of shale reaches 0.5-0.6, 5-10 MPa of pore pressure can cause rock fragmentation (Hou et al., 2016; Zhang et al., 2017; Wang et al., 2019). Due to the high brittleness index of samples B and C, excessive pore pressure can lead to the collapse of the pore network. Although the massive development of OM pores leads to an increase in micropores and the generation of bubble-like OM pores (**Fig. 20b, c, d**), such nanoscale pores contribute little to the total porosity of the shale (Guo et al., 2019), so the PV and SSA decrease at this stage. The change in sample A is different from that of the other samples due to the lower brittleness index. Therefore, in the mature to highly mature stage, the transformation from mesopores to macropores starts to occur in sample A, with macropores accounting for the major proportion, while the other samples are affected by the pore pressure and brittleness index, resulting in the compression of the pore space.

In stage IV (*Ro*=1.6%~3.0%), the changes in PV and SSA at this stage are mainly influenced by the hydrocarbon generation and the transformation of clay and halite minerals. From the highly mature stage to the overmature stage, OM cracked to produce gaseous hydrocarbons, leading to the development of amounts of OM pores and the appearance of spongy OM pores (**Fig. 20e, f**), with a large increase in the micropore PV and SSA. The dissolution of organic acids and transformation of clay minerals, such as the transformation of montmorillonite to illite (Peltonen et al., 2009; Hu et al., 2017; Peng, 2017) and dehydration of montmorillonite (Lanson et al., 1998, 2009) increase the PV and SSA of mesopores and macropores. Halite minerals mainly play two roles in this stage: as catalysts for hydrocarbon generation, halite minerals can promote the hydrocarbon generation and transformation of OM, resulting in halite minerals associated with OM significantly influencing the development of OM pores. The high thermal conductivity of halite minerals can reduce the activation energy of various reactions, thereby promoting the development of mesopores and macropores and the transformation of micropores-mesopores-macropores.

Fig. 20. The characteristics of OM pores under SEM in different stages: (a) In the mature stage, OM associated with halite minerals is more likely to produce OM pores under SEM; (b), (c), (d) In the high mature stage, bubble-like organic matter pores start to be produced; (e), (f) In the over mature stage, spongy OM pores start to be produced

6. Conclusions

(1) There are four main types of saline shale: interparticle pores, intraparticle pores, OM pores, and microfractures. Full pore size characterization of the shale was achieved by CO_2/N_2 adsorption and high-pressure mercury injection. The results showed that the contributions of PV and SSA were closely related to the gypsum-salt minerals, with macropores and mesopores providing the major PV and the contribution of SSA mainly provided by micropores. The shale with a high HC had a larger PV and SSA.

(2) There are two main occurrences of halite and gypsum minerals. One is the deposition of highly thick gypsum-salt rock, which is affected by deep thermal brine activity, sea erosion and arid environments.

The other is that OM is obviously associated with gypsum-salt minerals, and the halite minerals and gypsum minerals regularly occur around the OM. This deposition model is generated by the frequent alternation of humid and arid environments leading to the outbreak and death of organisms, resulting in large amounts of OM deposition and the precipitation of gypsum-salt minerals occurring simultaneously, forming the co-deposition of OM and gypsum-salt minerals.

(3) Gypsum-salt minerals play important roles in the formation and evolution of pores. With high brittleness and a high melting point, gypsum-salt minerals can form interparticle and intraparticle pores, which can accelerate the expulsion of hydrocarbons and increase the pore space of shale; gypsum-salt minerals can be used as catalysts for hydrocarbon generation by kerogen and promote the hydrocarbon transformation of OM, thus accelerating the generation of OM pores; with high thermal conductivity, the concentrated heat conduction of gypsum-salt minerals can reduce the activation energy of various chemical reactions, promote the development of various pores and improve the connectivity between pores.

(4) Based on the experimental results, the pore evolution model of shale with the participation of gypsum-salt rock was established. Stage I is mainly affected by mechanical compaction, which leads to an overall decrease in PV and SSA; stage II is affected by halite minerals and hydrocarbon generation, and the promotion of the hydrocarbon generation process by halite minerals is the reason for the frequent changes in PV and SSA; stage III is affected by pore pressure and the brittleness index. A higher brittleness index will cause the collapse of the pore network in the highly mature stage. Stage IV is influenced by OM hydrocarbon generation, clay mineral transformation and halite minerals. The 3 factors promote the development and transformation of the pore space simultaneously. Halite minerals play different roles in the mature stage and the overmature stage.

Acknowledgments We declare that we have no financial and personal relationships with other people or organizations that can inappropriately influence our work, there is no professional or other personal interest of any nature or kind in any product, service and/or company that could be construed as influencing the position presented in, or the review of, the manuscript entitled. This research was funded by the National Natural Science Foundation of China (41872128) and Postdoctoral Foundation of China University of Petroleum (Beijing) (ZX20220102). The authors thank the State Key Laboratory of Oil and Gas Resources and Exploration, China University of Petroleum (Beijing) for their support of this research.

References

Ahmed, K., Aya, A., Ahmed, R., et al., 2022. Paleoenvironment, sequence stratigraphy and source rock potentiality of the Cenomanian-Turonian boundary sediments of Southern Tethys. Mar. Pet. Geol. 105624-. https://doi.org/10.1016/J.MARPETGEO.2022.105624.

Barrett, E.P., Joyner, L.G., Halenda, P.P., 2002. The Determination of Pore Volume and Area Distributions in Porous Substances. I. Computations from Nitrogen Isotherms. J. Am. Chem. Soc. 73 (1), 373-380. https://doi.org/10.1021/ja01145a126.

Baruch, E.T., Kennedy, M.J., LöHr, S., et al., 2015. Feldspar dissolution-enhanced porosity in Paleoproterozoic shale reservoir facies from the Barney Creek Formation (McArthur Basin, Australia). AAPG (Am. Assoc. Pet. Geol.) Bull. 99 (9), 1745-1770. https://doi.org/10.1306/04061514181.

Bowker, K.A., 2007. Barnett Shale gas production, Fort Worth Basin: Issues and discussion. AAPG (Am. Assoc. Pet. Geol.) Bull. 91 (4), 523-533. https://doi.org/10.1306/06190606018.

Brunauer, S., Emmett, P.H., Teller, E., 1938. Adsorption of Gases in Multimolecular Layers. J. Am. Chem. Soc. 60 (2), 309-319. https://doi.org/10.1021/ja01269a023.

Cao, T.T., Liu, H., Pan, A.Y., et al., 2022. Pore evolution in siliceous shales and its influence on shale gas-bearing capacity in eastern Sichuan-western Hubei, China. J. Petrol. Sci. Eng. 208 (PC). https://doi.org/10.1016/J.PETROL.2021.109597.

Chalmers, G.R., Bustin, R.M., 2008. Lower Cretaceous gas shales in northeastern British Columbia, Part I: geological controls on methane sorption capacity. Bull. Can. Petrol. Geol. 56, 1-21. https://doi.org/10.2113/gscpgbull.56.1.1.

Chalmers, G.R., Bustin, R.M., Power, I.M., 2012. Characterization of gas shale pore systems by porosimetry, pycnometry, surface area, and field emission scanning electron microscopy/transmission electron microscopy image analyses: Examples from the Barnett, Woodford, Haynesville, Marcellus, and Doig units. AAPG (Am. Assoc. Pet. Geol.) Bull. 96, 1099-1119. https://doi.org/10.1306/10171111052.

Chen, D., Pang, X.Q., Jiang, F.J., et al., 2021b. Shale Oil Potential and Mobility of Low-Maturity Lacustrine Shales: Implications from NMR Analysis in the Bohai Bay Basin. Energy Fuels 35 (3), 2209-2223. https://doi.org/10.1021/ACS.ENERGYFUELS.0C03978.

Chen, D., Pang, X.Q., Li, L., et al., 2021a. Organic geochemical characteristics and shale oil potential of the middle Eocene early-mature shale in the Nanpu Sag, Bohai Bay Basin, Eastern China. Mar. Pet. Geol. (4), 105248. https://doi.org/10.1016/J.MARPETGEO.2021.105248.

Chen, D., Pang, X.Q., Wang, Y., et al., 2020. Palaeoenvironmental periodisms of middle Eocene terrestrial sediments in Bohai Bay Basin, eastern China, and their implications for organic matter accumulation. Mar. Pet. Geol. 112 (C), 104060-104060. https://doi.org/10.1016/j.marpetgeo.2019.104060.

Chen, F.L., Zhu, H., Li, X.T., et al., 2000. Partition of Sequence Strata and Discussion about Salt-rock Resource in Shahejie Formation of Eogene, Dongpu Depression. Acta Sedimentol. Sin. (03), 384-388. https://doi.org/10.14027/j.cnki.cjxb.2000.03.010.

Chen, J., Jiang, F.J., Hu, T., et al., 2016. Experimental investigation of the characteristics of organic matter pores in Chang 7 member lacustrine shale from the Ordos Basin due to organic matter evolution induced by hydrous pyrolysis. J. Nat. Gas. Sci. Eng. 35, 412-424. https://doi.org/10.1016/j.jngse.2016.08.069.

Chen, J., Lu, K., Feng, Y., et al., 2012. Evaluation of hydrocarbon source rocks in different environments and characteristics of hydrocarbon generation and expulsion in Dongpu Depression. Fault-Block Oil Gas Field 19 (01), 35-38. https://doi.org/10.6056/dkyqt201201008.

Chen, J., Xiao, X.M., 2014. Evolution of nanoporosity in organic-rich shales during thermal maturation. Fuel 129, 173-181. https://doi.org/10.1016/j.fuel.2014.03.058.

Debanjan, C., Tuli, B., Vikram, V., 2021. Thermal effect on pore characteristics of shale under inert and oxic environments: Insights on pore evolution. Microporous Mesoporous Mater. 316. https://doi.org/10.1016/J.MICROMESO.2021.110969.

Ding, T., Liu, C.L., Zhao, Y.J., et al., 2019. Chlorine isotope analysis of Triassic salt rock and geological significance of ancient salt lake in Sichuan Basin, China. Carbonates Evaporites 34 (3), 909-915. https://doi.org/10.1007/s13146-018-0431-4.

Du, H.F., Yu, X.H., Chen, F.L., 2008. Sedimentary characteristics of saltrocks and their petroleum geologic significance of the Member 3 of Shahejie Formation of Paleogene in Dongpu Sag, Henan Province. J. Palaeogeogr. 10 (1), 53-62. https://doi.org/10.7605/gdlxb.2008.01.006.

Dubinin, M., Stoeckli, H., 1980. Homogeneous and heterogeneous micropore structures in carbonaceous adsorbents. J. Colloid. Interface. Sci. 75 (1), 34-42. https://doi.org/10.1016/0021-9797(80)90346-X.

Edgell, H.S., 1996. Salt tectonism in the Persian Gulf basin. Spec. Publ. Geol. Soc. 100 (1), 129-151. https://doi.org/10.1144/gsl.sp.1996.100.01.10.

Edward, W.W., 1921. The Dynamics of Capillary Flow. Proc. Am. Phys. Soc. 17 (3), 273. https://doi.org/10.1103/PhysRev.17.273.

Eyong, J.T., Gabriel, N., Moïse, B., et al., 2018. Sedimentologic and palaeoenvironmental evolution of the Mamfe Cretaceous Basin (SW Cameroon): Evidence from lithofacies analysis, tectonics and evaporite minerals suite. J. Afr. Earth Sci. 149, 19-41. https://doi.org/10.1016/j.jafrearsci.2018.07.022.

Gao, H.C., Chen, F.L., Liu, G.R., et al., 2009. Advance, problems and prospect of origin of salt rocks of Paleogene Shahejie Formation in Dongpu Sag. J. Palaeogeogr. 11(03), 251-264. https://doi.org/10.7605/gdlxb.2009.03.001.

Gao, H.C., Zheng, R.C., Xiao, Y.K., et al., 2015. Origin of the salt rock of Paleogene Shahejie Formation in Dongpu Sag, Bohai Bay Basin: evidences from Sedimentology and geochemistry. Acta Pet. Sin. 36 (01), 19-32. https://doi.org/10.7623/syxb201501003.

Gong, S.Y., 2020. Evolutional Characteristics of Evaporites-bearing Shale Pore Structure in Dongpu Depression and its quantitative characterization. China University Of Petroleum (Beijing) https://doi.org/10.27643/d.cnki.gsybu.2020.000460.

Gregg, S.J., Sing, K.S.W., Salzberg, H.W., 2019. Adsorption Surface Area and Porosity. J. Electrochem. Soc. 114 (11), 279C-279C. https://doi.org/10.1149/1.2426447.

Gu, Y.T., Li, X.X., Wan, Q., et al., 2021. On the Different Characteristics of Organic Pores in Shale and Their Influencing Factors: Taking typical marine, continental, and transitional facies reservoirs in China as examples. Acta Sedimentol. Sin. 39 (04), 794-810. https://doi.org/j.issn.1000-0550.2020.134.

Guan, M., Liu, X.P., Jin, Z.J., et al., 2022 The evolution of pore structure heterogeneity during thermal maturation in lacustrine shale pyrolysis. J. Anal. Appl. Pyrolysis 105501-. https://doi.org/10.1016/J.JAAP.2022.105501.

Guo, H.J., Jia, W.L., Peng, P.A., et al., 2017. Evolution of organic matter and nanometer-scale pores in an artificially matured shale undergoing two distinct types of pyrolysis: A study of the Yanchang Shale with Type II kerogen. Org. Geochem. 105, 56-66. https://doi.org/10.1016/j.orggeochem.2017.01.004.

Guo, P., 2018. Saline environment evolution of the Cenozoic Qaidam Palaeolake and the characterizarion of its hydrocarbon source rocks. Northwestern University (in Chinese).

Guo, P., Li, C.Y., 2022. Genesis of evaporites in petroliferous basins and the sedimentary and climatic significances. J. Palaeogeogr. 24 (02), 210-225. https://doi.org/10.7605/gdlxb.2022.02.016.

Guo, S.B., Mao, W.J., 2019. Division of diagenesis and pore evolution of a Permian Shanxi shale in the Ordos Basin, China J. Petrol. Sci. Eng. 182 (C), 106351-106351. https://doi.org/10.1016/j.petrol.2019.106351.

Han, Y., Chen, Y., 2015. Research progress on microscopic characteristics of salt-bearing shale. Geol. Rev. 61 (S1), 645-646 (in Chinese).

Hao, F., Dong, W.L., Zou, H.Y., et al. 2003. Overpressure fluid flow and rapid accumulation of natural gas in Yinggehai Basin. Acta Pet. Sin. (06), 7-12. https://doi.org/10.7623/syxb200306002.

He, R.L., Jia, W.L., Peng, P.A., 2018. Influence of hydrocarbon expulsion and retention on the evolution of nanometer-scale pores in organic matter rich shale: An example from pyrolysis experiment. Acta Geochim. 47 (05), 575-585. https://doi.org/10.19700/j.0379-1726.2018.05.009.

He, W.Y., Bai, X.F., Meng, Q.A., et al., 2022. Accumulation geological characteristics and major discoveries of lacustrine shale oil in Sichuan Basin. Acta Pet. Sin. 43(07), 885-898. https://doi.org/10.7623/syxb202207001.

Hou, Z.K., Yang, C.H., Wang, L., et al., 2016. Evaluation Method of Shale Brittleness Based on Indoor Experiments. J. Northeast Univ. Nat. Sci. 37 (10), 6. https://doi.org/10.3969/j.issn.1005-3026.2016.10.027.

Hu, H.Y., Hao, F., Lin, J.F., et al., 2017. Organic matter-hosted pore system in the wufeng-Longmaxi (O3w-S11) shale, Jiaoshiba area, eastern Sichuan basin, China. Int. J. Coal Geol. 173, 40-50. https://doi.org/10.1016/j.coal.2017.02.004.

Hu, T., Pang, X.Q., Jiang, F.J., et al., 2021a. Factors Controlling Differential Enrichment of Organic Matter in Saline Lacustrine Rift Basin: A case study of third member Shahejie Fm in Dongpu Depression. Acta Sedimentol. Sin. 33 (01), 140-152. https://doi.org/10.14027 / j.i SSN. 1000-0550.2020.125.

Hu, T., Pang, X.Q., Jiang, F.J., et al., 2021b. Key factors controlling shale oil enrichment in saline lacustrine rift basin: implications from two shale oil wells in Dongpu Depression, Bohai Bay Basin. Pet. Sci. 1-25. https://doi.org/10.1007/S12182-021-00564-Z.

Hu, T., Pang, X.Q., Jiang, F.J., et al., 2021c. Movable oil content evaluation of lacustrine organic-rich shales: Methods and a novel quantitative evaluation model. Earth Sci. Rev. 214. https://doi.org/10.1016/J.EARSCIREV.2021.103545.

Hu, T., Pang, X.Q., Jiang, F.J., et al., 2022a. Dynamic continuous hydrocarbon accumulation (DCHA): Existing theories and a new unified accumulation model. Earth Sci. Rev. 232. https://doi.org/10.1016/J.EARSCIREV.2022.104109.

Hu, T., Pang, X.Q., Xu, T.W., et al., 2022b. Identifying the key source rocks in heterogeneous saline lacustrine shales: Paleogene shales in the Dongpu depression, Bohai Bay Basin, eastern China. AAPG (Am. Assoc. Pet. Geol.) Bull. 106 (6), 1325-1356. https://doi.org/10.1306/01202218109.

Huang, Y.Q., Zhang, J.C., Zhang, P., et al., 2016. Microscopic Characteristics and Main Controlling Factors of Shale Reservoir Space of Es_3 Formation, Northern Dongpu Depression. J. Shandong Univ. Sci. Technol. Nat. Sci. 35 (03), 8-16. https://doi.org/10.3969/j.issn.1672-3767.2016.03.002.

Huang, Z.K., Chen, J.P., Wang, Y.J., et al., 2013. Characteristics of micropores in mudstones of the Cretaceous Qingshankou Formation,Songliao Basin. Acta Pet. Sin. 34 (01), 30-36. https://doi.org/10.7623/syxb201301004.

Hudec, M.R., Jackson, M.P.A., 2006. Advance of allochthonous salt sheets in passive margins and orogens. AAPG (Am. Assoc. Pet. Geol.) Bull. 90 (10), 1535-1564. https://doi.org/10.1306/05080605143.

Jarvie, D.M., Hill, R.J., Ruble, T.E., et al., 2007. Unconventional shale gas systems: The Mississippian Barnett Shale of north-central Texas as one modle for thermogenic shale-gas assessment. AAPG (Am. Assoc. Pet. Geol.) Bull. 91 (4), 475-499. https://doi.org/10.1306/12190606068.

Ji, Y.L., Feng, J.H., Wang, S.L., et al., 2005. Origin of Salt and Gypsum Rock in the Third Member of Shahejie Formation of Lower Tertiary in Dongpu Depression. Acta Sedimentol. sin. 23 (2), 225-231. https://doi.org/10.3969/j.issn.1000-0550.2005.02.006.

Jiang, F.J., Chen, D., Wang, Z., et al., 2016. Pore characteristic analysis of a lacustrine shale: A case study in the Ordos Basin, NW China. Mar. Pet. Geol. 73, 554-571. https://doi.org/10.1016/j.marpetgeo.2016.03.026.

Jiang, F.J., Chen, D., Zhu, C.X., et al., 2022. Mechanisms for the anisotropic enrichment of organic matter in saline lake basin: A case study of the Early Eocene Dongpu Depression, eastern China J. Petrol. Sci. Eng. 210. https://doi.org/10.1016/J.PETROL.2021.110035.

Jiang, F.J., Chen, J., Xu, Z.Y., et al., 2017. Organic Matter Pore Characterization in Lacustrine Shales with Variable Maturity Using Nanometer-Scale Resolution X-ray Computed Tomography. Energy Fuels 31 (3), 2669-2680. https://doi.org/10.1021/acs.energyfuels.6b03313.

Jiang, F.J., Huang, R.D., Hu, T., et al., 2022. Geological characteristics and classification evaluation of shale oil in Fengcheng Formation in Mahu sag, Junggar Basin. Acta Pet. Sin. 43 (07), 899-911. https://doi.org/10.7623/syxb202207002.

Jiang, F.J., Wang, Q.F., Liu, L., et al., 2018. Geological and geochemical characteristics of the Middle-Lower Jurassic shales in the Kuqa Depression, Tarim Basin: an evaluation of shale gas resources. Aust. J. Earth Sci. 65 (4), 557-573. https://doi.org/10.1080/08120099.2018.1447014.

Jiang, F.J., Zhang, C.L., Wang, K., et al., 2019. Characteristics of micropores, pore throats, and movable fluids in the tight sandstone oil reservoirs of the Yanchang Formation in the southwestern Ordos Basin, China. AAPG (Am. Assoc. Pet. Geol.) Bull. 103 (12), 2835-2859. https://doi.org/10.1306/03061917284.

Jin, Q., Huang, X.H., 1985. Studies on the origin of early tertiary salt lake Dongpu Depression: A postulated deep water model. J. China Univ. Pet. Ed. Nat. Sci. 9 (1), 1-11 (in Chinese).

Jin, Q., Zha, M., 2000. Co-sedimentation of tertiary evaporites and oil source rocks in the Western Qaidam Basin. Sci. Geol. Sin. (04), 465-473. https://doi.org/10.3321/j.issn:0563-5020.2000.04.010.

Jin, Q., Zhu, G.Y., Wang, J., 2008. Deposition and distribution of high-potential source rocks in saline lacustrine environments. J. China Univ. Pet. Ed. Nat. Sci. 32 (4), 19-23. https://doi.org/10.3321/j.issn:1673-5005.2008.04.004.

Jin, Z.J., Bai, Z.K., Gao, B., et al., 2019. Has China ushered in the shale oil and gas revolution? Oil Gas Geol. 40 (03), 451-458. https://doi.org/10.11743/ogg20190301.

Ko, L.T., Loucks, R.G., Zhang, T.W., et al., 2016. Pore and pore network evolution of Upper Cretaceous Boquillas (Eagle Ford–equivalent) mudrocks: Results from gold tube pyrolysis experiments. AAPG (Am. Assoc. Pet. Geol.) Bull. 100 (11), 1693-1722. https://doi.org/10.1306/04151615092.

Kuang, L.C., Hou, L.H., Yang, Z., et al., 2021. Key parameters and methods of lacustrine shale oil reservoir characterization. Acta Pet. Sin. 42 (01), 1-14. https://doi.org/10.7623/syxb202101001.

Kuila, U., Prasad, M., 2013. Specific surface area and pore-size distribution in clays and shales. Geophys. Prospect. 61 (2), 341-362. https://doi.org/10.1111/1365-2478.12028.

Lanson, B., Sakharov, B.A., Claret, F., 2009. Diagenetic smectite-to-illite transition in clay-rich sediments: a reappraisal of X-ray diffraction results using the multi-specimen method. Am J Sci. 309 (6), 476-516.

Lanson, B., Velde, B., Meunier, A., 1998. Late-stage diagenesis of illitic clay minerals as seen by decomposition of X-ray diffraction patterns: Contrasted behaviors of sedimentary basins with different burial histories. Clays Clay Miner. 46 (1), 69-78. https://doi.org/10.1346/CCMN.1998.0460108.

Li, B., 2018. Origin of salt rocks of Shahejie Formation and its relationship with source Rocks in Dongpu Depression. Northwest University (in Chinese).

Li, C.Z., Guo, P., Liu, C.Y., 2021. Deposition models for the widespread Eocene bedded halite in China and their implications for hydrocarbon potential of salt-associated mudstones. Mar. Pet. Geol. 05132-. https://doi.org/10.1016/J.MARPETGEO.2021.105132.

Li, G.S., Wang, Y.B., Lu, Z.S., et al., 2014. Geobiological processes of the formation oflacustrine source rock in Paleogene. Sci. China Earth Sci. 57 (5), 976-987. https://doi.org/10.1007/s11430-013-4753-8.

Li, H.L., Zhang, Y.X., Zhou, Y.S., et al., 2020. Hydrocarbon evolution mechanism of high quality source rock in Dongpu Sag. Fault-Block Oil Gas Field 27 (2), 143-148. https://doi.org/10.6056/dkyqt202002002.

Li, L., Ti, X.C., Cao, J., et al., 2014. Origins of evaporites in the Middle Triassic Leikoupo Formation of the Sichuan Basin, southwest China and their geological implications. Carbonates Evaporites 29 (1), 55-63. https://doi.org/10.18654/1000-0569/2019.04.12.

Liang, Z.Z., Yu, T.H., 2016. Research status and exploration enlightenment on over pressure and enrichment shale gas in North America. Coal Sci. Technol. 44 (10), 161-166. https://doi.org/10.13199/j.cnki.cst.2016.10.030.

Liu, J.D., Jiang, Y.L., Tan, Y.M., et al., 2014. Relationship between Gypsum-salt Rock and Oil-gas in Dongpu Depression of Bohai Gulf Basin. Acta Sedimentol. Sin. 32 (01), 126-137. https://doi.org/10.14027/j.cnki.cjxb.2014.01.015.

Liu, R.B., 2015. Analyses of influences on shale reservoirs of Wufeng-Longmaxi Formation by overpressure in the Sichuan Basin. Acta Sedimentol. Sin. 33 (4), 817-827. https://doi.org/10.14027/j.cnki.cjxb.2015.04.020.

Liu, X.P., Li, W.Q., 2020. Research Advance on Pore Evolution of Organic-rich Shale Based on Thermal Simulation Experiment. Sci. Tech. Eng. 20 (22), 8849-8859. https://doi.org/10.3969/j.issn.1671-1815.2020.22.002.

Liu, X.W., Wang, X.J., Li, H.L., et al., 2021. Characteristics and formation environment analysis of Paleogene source rocks in Dongpu Depression. Fault-block Oil Gas Field 28 (4), 452-455. https://doi.org/10.6056/dkyqt202104004.

Loucks, R.G., Reed, R.M., 2014. Abstract: Scanning-Electron-Microscope Petrographic Evidence for Distinguishing Organic-Matter Pores Associated with Depositional Organic Matter versus Migrated Organic Matter in Mudrocks. Gcags Transactions 3, 51-60.

Loucks, R.G., Reed, R.M., Ruppel, S., 2012. Spectrum of pore types and networks in mudrocks and a descriptive classification for matrix-related mudrock pores. AAPG (Am. Assoc. Pet. Geol.) Bull. 96, 1071-1098. https://doi.org/10.1306/08171111061.

Loucks, R.G., Reed, R.M., Ruppel, S.C., et al., 2009. Morphology, genesis, and distribution of nanometer-scale pores in siliceous mudstones of the Mississippian Barnett Shale. J. Sediment. Res. 79, 848-861. https://doi.org/10.2110/jsr.2009.092.

Lu, S.F., Xue, H.T., Wang, M., et al., 2016. Several key issues and research trends in evaluation of shale oil. Acta Pet. Sin. 37 (10), 1309-1322. https://doi.org/10.7623/syxb201610012.

Luo, R., Cha, M., He, H., et al., 2017. Effect of mineral dissolution by organic acids on pore structure of shale reservoir. J. China Univ. Pet. Ed. Nat. Sci. 41 (02), 49-59. https://doi.org/10.3969/j.issn.1673-5005.2017.02.006.

Luo, Y., Zhao, Y., Lv, X., 2013. Characterization of the upper Es_3, inter-salt shale reservoir in Liutun sag, Dongpu depression. Acta Pet. Sin. 34 (02), 293-300. https://doi.org/10.7623/syxb201302011.

Ma, X., Hua, A., Li, J., et al., 2000. Salt oil and gas basin. Beijing: Petroleum Industry Press. 1-110 (in Chinese).

Ma, Z., Zheng, L., Li, Z., et al., 2013. The Effect of Salts on Hydrocarbon Generation and Expulsion of Argillaceous Source Rock. J. Southwest Pet. Univ. Sci. Technol. Ed. 35 (01), 43-51. https://doi.org/10.3863/j.issn.1674 – 5086.2013.01.006.

Ma, Z.L., Zheng, L.J., Xu, X.M., et al., 2017. Thermal simulation experiment on the formation and evolution of organic pores in organic-rich shale. Acta Pet. Sin. 38 (01), 23-30. https://doi.org/10.7623/syxb201701003.

Mahmoud, A.A., Rushdi, J.T., Ammar, A.M., 2020. Sedimentological implications of microbial mats, gypsum, and halite in Dhahban solar saltwork, Red Sea coast, Saudi Arabia. Facies 66 (2), 10. https://doi.org/10.1007/s10347-020-0594-z.

Martini, A.M., Walter, L.M., Ku, T.C.W., et al., 2003. Microbial production and modification of gases in sedimentary basins: A geochemical case study from a Devonian shale gas play, Michigan basin. AAPG (Am. Assoc. Pet. Geol.) Bull. 87 (8), 1355-1375. https://doi.org/10.1306/031903200184.

Mastalerz, M., Schimmelmann, A., Drobniak, A., et al., 2013. Porosity of Devonian and Mississippian New Albany Shale across a maturation gradient: insights from organic petrology, gas adsorption, and mercury intrusion. AAPG (Am. Assoc. Pet. Geol.) Bull. 97, 1621-1643. https://doi.org/10.1306/04011312194.

Mastalerz, M., Wei, L., Drobniak, A., et al., 2018. Responses of specific surface area and micro- and mesopore characteristics of shale and coal to heating at elevated hydrostatic and lithostatic pressures. Int. J. Coal Geol. 197, S0166516218302003-. https://doi.org/10.1016/j.coal.2018.06.026.

Milliken, K.L., Rudnicki, M., Awwiller, D.N., et al., 2013. Organic matter-hosted pore system, Marcellus Formation (Devonian), Pennsylvania. AAPG (Am. Assoc. Pet. Geol.) Bull. 97 (2), 177-200. https://doi.org/10.1306/07231212048.

Peltonen, C., Marcussen, Y., Bjrlykke, K., et al., 2008. Clay mineral diagenesis and quartz cementation in mudstones: The effects of smectite to illite reaction on rock properties. Mar. Pet. Geol. 2009;26 (6):887-898. https://doi.org/10.1016/j.marpetgeo. 01, 021.

Peng, C., Pan, J.N., Wan, X.Q., et al., 2017. Effect of clay minerals of coal-bearing shale on pore structure and methane adsorption property in Yuzhou coalfield. J. China Coal Soc. (6), 46-52. https://doi.org/10.19880/j.cnki.ccm.2017.06.009.

Peng, J.C., Zhang, Y., Zhang, X.Q., et al., 2014. History and prospect of presalt oil-gas exploration in the salt basin of the world. China Mining Magazine 23 (S2), 114-117. https://doi.org/10.3969/j.issn.1004-4051.2014.z2.030.

Reed, R.M., Loucks, R.L., Ko, L.T., 2020. Scanning Electron Microscope Petrographic Differentiation among Different Types of Pores Associated with Organic Matter in Mudrocks. Gulf. Coast Assoc. Geol. Soc. Trans. 9, 17-27.

Ross, D.J.K., Bustin, R.R.M., 2008a. Characterizing the shale gas resource potential of Devonian- Mississippian strata in the Western Canada sedimentary basin: Application of an integrated formation evaluation. AAPG (Am. Assoc. Pet. Geol.) Bull. 92 (1), 87-125. https://doi.org/10.1306/09040707048.

Ross, D.J.K., Bustin, R.M., 2008b. The importance of shale composition and pore structure upon gas storage potential of shale gas reservoirs. Mar. Petrol. Geol. 26, 916-927. https://doi.org/10.1016/j.marpetgeo.2008.06.004.

Schneider, A.C., Mutterlose, J., Blumenberg, M., et al., 2019. Palynofacies, micropalaeontology, and source rock evaluation of non-marine Jurassic-Cretaceous boundary deposits from northern Germany - Implications for palaeoenvironment and hydrocarbon potential. Mar. Pet. Geol. 103, 526-548. https://doi.org/10.1016/j.marpetgeo.2019.02.016.

Shao, X.H., Pang, X.Q., Hu, T., 2019. Microscopic characteristics of pores in Es_3 shales and its significances for hydrocarbon retention in Dongpu Sag, Bohai Bay Basin. Oil Gas Geol. 40 (01), 67-77. https://doi.org/10.11743/ogg20190107.

Shao, X.H., Pang, X.Q., Li, H., et al., 2018. Pore network characteristics of lacustrine shales in the Dongpu Depression, Bohai Bay Basin, China, with implications for oil retention. Mar. Pet. Geol. 96, 457-473. https://doi.org/10.1016/j.marpetgeo.2018.06.015.

Shen, Z.M., Ye, S.J., Ma, Q.M., 2001. Main organic geochemical characteristics of low-mature oils in China. J. Chengdu Univ. Technol. (04), 396-401. https://doi.org/10.3969/j.issn.1671-9727.2001.04.013.

Shi, X.F., 2008. Study of Sequence Stratigraphy and Favorable Reservoir Predication for Es_3 Formation in the North of Dongpu Depression. China University of Geosciences (Beijing) (in Chinese).

Souza, F.Y., Maria, F.R., Paula, L.A., 2022. New paleoenvironmental and palynostratigraphic data from Solimões Formation (Solimões Basin, Amazonas, Brazil). J. South Am. Earth Sci. 115. https://doi.org/10.1016/J.JSAMES.2022.103751.

Su, H., Qu, L.P., Zhang, J.C., et al., 2006. Tectonic evolution and extensional pattern of rifted basin: a case study of Dongpu depression. Oil Gas Geol. (01), 70-77. https://doi.org/10.3321/j.issn:0253-9985.2006.01.012.

Sun, L., Tuo, J.C., Zhang, M.F., et al., 2015. Formation and development of the pore structure in Chang 7 member oil-shale from Ordos Basin during organic matter evolution induced by hydrous pyrolysis. Fuel 158, 549-557. https://doi.org/10.1016/j.fuel.2015.05.061.

Surdam, R.C., Crossey, L.G., Eglinton, G., et al., 1985. Organic-inorganic reactions during progressive burial: key to porosity and permeability enhancement and preservation [and discussion]. Phil. Trans. Roy. Soc. Lond. 315, 135-156. https://doi.org/10.1098/rsta.1985.0034.

Sweeney, J., Burnham, A.K., 1990. Evaluation of a simple model of vitrinite reflectance based on chemical kinetics. AAPG (Am. Assoc. Pet. Geol.) Bull. 74 (10), 1559-1570. https://doi.org/10.1306/0c9b251f-1710-11d7-8645000102c1865d.

Tang, L.J., Yu, Y.X., Chen, S.P., et al., 2005. Major developments of research on salt tectonics in oil gas bearing basins. Earth Sci. Front. 12 (4), 375-383. https://doi.org/10.3321/j.issn:1005-2321.2005.04.006.

Tang, X.H., 1990. Oil and gas resources in saline basins around the world. Geol. China (07), 27-28.

Tao, C., Yin, J., Liu, J., et al., 2015. Characteristics of hydrocarbon distribution in saline basins of the passive land margin in the South Atlantic. Geol. Rev. 61 (S1), 168-169 (in Chinese).

Tenger, B., Lu, L.F., Yu, L.J., et al., 2021. Formation, preservation and connectivity control of organic pores in shale. Pet. Explor. Dev. 48 (04), 798-812. https://doi.org/10.11698/PED.2021.04.02.

Tian, H., Zhang, S.C., Liu, S.B., et al., 2012. Determination of organic-rich shale pore features by mercury injection and gas adsorption methods. Acta Petrol. Sin. 33 (3), 419-427. https://doi.org/10.7623/syxb201203011.

Triine, N., Ieva, G., Edyta, K., et al., 2022. Late-Holocene relative sea-level changes and palaeoenvironment of the Pre-Viking Age ship burials in Salme, Saaremaa Island, eastern Baltic Sea. The Holocene. 32 (4), 237-253. https://doi.org/10.1177/09596836211066596.

Ulisses, T., Carry, K., 1996. Development of sediment overpressure and its effective thermal maturation: application to the Gulf of Mexico Basin. AAPG (Am. Assoc. Pet. Geol.) Bull. 9, 1367-1396. https://doi.org/10.1029/95GL00085.

Utrilla, R., Pierre, C., Orti, F., et al., 1992. Oxygen and sulphur isotope compositions as indicators of the origin of Mesozoic and Cenozoic evaporites from spain. Chem. Geol. 102 (1-4), 229-244. https://doi.org/10.1016/0009-2541(92)90158-2.

Waele, J.D., Picotti, V., Martina, M.L.V., et al., 2020. Holocene evolution of halite caves in the Cordillera de la Sal (Central Atacama, Chile) in different climate conditions. Geomorphol. 370. https://doi.org/10.1016/j.geomorph.2020.107398.

Wang, F.T., Guo, S.B., 2019. Influential factors and model of shale pore evolution: A case study of a continental shale from the Ordos Basin. Mar. Pet. Geol. 102, 271-282. https://doi.org/10.1016/j.marpetgeo.2018.12.045.

Wang, J.X., Hu, Z.G., Li, S.L., et al., 2022. Distribution characteristics and sedimentary model of gypsum-bearing evaporite of the Middle Cambrian Gaotai Formation in the eastern Sichuan Basin. Arabian J. Geosci. 15 (11). https://doi.org/10.1007/S12517-022-10286-0.

Wang, Q.F., Jiang, F.J., Ji, H.C., et al., 2020a. Differential Enrichment of Organic Matter in Saline Lacustrine Source Rocks in a Rift Basin: A Case Study of Paleogene Source Rocks, Dongpu Depression, Bohai Bay Basin. Nat. Resour. Res. 29 (1-2), 1-20. https://doi.org/10.1007/s11053-020-09671-x.

Wang, Q.F., Jiang, F.J., Ji, H.C., et al., 2020b. Effects of paleosedimentary environment on organic matter enrichment in a saline lacustrine rift basin - A case study of Paleogene source rock in the Dongpu Depression, Bohai Bay Basin. J. Petrol. Sci. Eng. 195. https://doi.org/10.1016/j.petrol.2020.107658.

Wang, W.Y., Pang, X.Q., Chen, Z., et al., 2019. Quantitative prediction of oil and gas prospects of the Sinian-Lower Paleozoic in the Sichuan Basin in central China. Energy 174, 861-872. https://doi.org/10.1016/j.energy.2019.03.018.

Wang, W.Y., Pang, X.Q., Chen, Z., et al., 2020. Improved methods for determining effective sandstone reservoirs and evaluating hydrocarbon enrichment in petroliferous basins. Appl. Energy 261 (C), 114457-114457. https://doi.org/10.1016/j.apenergy.2019.114457.

Wang, W.Y., Pang, X.Q., Wang, Y.P., et al., 2022. Hydrocarbon expulsion model and resource potential evaluation of high-maturity marine source rocks in deep basins: Example from the Ediacaran microbial dolomite in the Sichuan Basin, China. Pet. Sci. 19 (6), 2618-2630. https://doi.org/10.1016/J.PETSCI.2022.11.018.

Wang, Y., 2019. Rock brittleness index and its numerical simulation in SRV fracturing. Pet. Geol. Oilfield Dev. Daqing 38 (4), 76-81. https://doi.org/10.19597/j.issn.1000-3754.201811066.

Wang, Y., Zhu, Y., Wang, H., et al., 2015. Nanoscale pore morphology and distribution of lacustrine shale reservoirs： Examples from the Upper Triassic Yanchang Formation, Ordos Basin. J. Energy Chem. 24 (4), 512-519. https://doi.org/10.1016/j.jechem.2015.06.004.

Washburn, E.W., 1921. The Dynamics of Capillary Flow. Phys. Rev. Ser. 17 (3), 273-283. https://doi.org/10.1103/PhysRev.17.273.

Wu, S.T., Yang, Z.Y., Zhai, X.F., et al., 2019. An experimental study of organic matter, minerals and porosity evolution in shales within high-temperature and high-pressure constraints. Mar. Pet. Geol. 102, 377-390. https://doi.org/10.1016/j.marpetgeo.2018.12.014.

Xiao, J.L., Li, Y.Z., Hou, Z.K., 2017. Evaluation method for shale reservoir brittleness. Fault-block Oil Gas Field 24 (04), 486-489. https://doi.org/10.6056/dkyqt201704011.

Xiong, Y., Tan, X.C., Wu, K.Y., et al., 2021. Petrogenesis of the Eocene lacustrine evaporites in the western Qaidam Basin: Implications for regional tectonic and climate changes. Sediment. Geol. 416. https://doi.org/10.1016/J.SEDGEO.2021.105867.

Xu, J.L., Wu, S.T., Liu, J.D., et al., 2021. New Insights into Controlling Factors of Pore Evolution in Organic-rich Shale. Energy Fuels 35 (6), 4858-4873. https://doi.org/10.1021/ACS.ENERGYFUELS.0C04189.

Xu, L., Yang, K., Lu, W., et al., 2022. New Research Progress on Organic-rich Shale Micro- and Nanoscale Pore System Evolution Characteristics and Models. J. Sediment. 40 (01), 1-21. https://doi.org/10.14027/j.issn.1000-0550.2020.085.

Xu, L.W., Yang, K.J., Wei, H., et al., 2021. Pore evolution model and diagenetic evolution sequence of the Mesoproterozoic Xiamaling shale in Zhangjiakou, Hebei. J. Petrol. Sci. Eng. 207. https://doi.org/10.1016/J.PETROL.2021.109115.

Yan, K., Liu, C.L., Wang, C.L., et al., 2021. Mineral deposition and paleoenvironment of Cretaceous evaporite in Southwestern Congo. Acta Petrol. Mineral 40 (03), 525-534. https://doi.org/10.3969/j.issn.1000-6524.2021.03.006.

Yang, X., 2007. The study of source rock and hydrocarbon's geochemistry characteristic of Member one of Shahejie Formation in Dongpu Sag. Chengdu University of Technology (in Chinese).

Zhang, J., Ai, C., Li, Y.W., et al., 2017. Brittleness evaluation index based on energy variation in the whole process of rock failure. Chin. J. Rock Mech. Eng. 4 (6), 1326-1340. https://doi.org/10.13722/j.cnki.jrme.2016.0839.

Zhang, S., Liu, H.M., Wang, M., et al., 2018. Pore evolution of shale oil reservoir in Dongying sag. Acta Petrol. Sin. 39 (07), 754-766. https://doi.org/10.7623/syxb201807003.

Zhang, Y.X., Xu, C., 2019. Characteristics and Generation Potential of Paleogene Hydrocarbon Organisms in the Dongpu Sag. Geol. J. China Univ. 25 (6), 10. https://doi.org/10.16108/j.issn1006-7493.2019087.

Zheng, T.Y., Zieger, L., Baniasad, A., et al., 2022. The Shahejie Formation in the Dongpu Depression, Bohai Bay Basin, China: Geochemical investigation of the origin, deposition and preservation of organic matter in a saline lacustrine environment during the Middle Eocene. Int. J. Coal Geol. 103967-. https://doi.org/10.1016/J.COAL.2022.103967.

Zhu, C.X., Jiang, F.J., Zhang, P.Y., et al., 2021. Identification of effective source rocks in different sedimentary environments and evaluation of hydrocarbon resources potential: A case study of paleogene source rocks in the Dongpu Depression, Bohai Bay Basin. J. Petrol. Sci. Eng. 201. https://doi.org/10.1016/J.PETROL.2021.108477.

Zou, C.N., Dong, D.Z., Wang, S.J., et al., 2010. Geological characteristics formation mechanism and resource potential of shale gas in China. Pet. Explor. Dev. 37 (6), 641-653. https://doi.org/10.1016/S1876-3804(11)60001-3.

Zou, C., Pan, S.Q., Zhao, Q., 2020. On the connotation, challenge and significance of China's "energy independence" strategy. Pet. Explor. Dev. 47 (02), 416-426. https://doi.org/10.11698/PED.2020.02.21.

Zou, C.N., Zhu, R.L., Dong, D.Z., et al., 2022. Scientific and technological progress, development strategy and policy suggestion regarding shale oil and gas. Acta Petrol. Sin. 43 (12), 1675-1686. https://doi.org/10.7623/syxb202212001.

Zuo, Z.F., Xiong, Y., He, W., et al., 2019. Diagenesis and Porosity Evolution of the Subsalt Member 5 of Majiagou Formation Reservoir in the Central Ordos Basin. Geol. Sci. Technol. Inf. 42 (5), 155-164. https://doi.org/10.19509/j.cnki.dzkq.2019.0516.

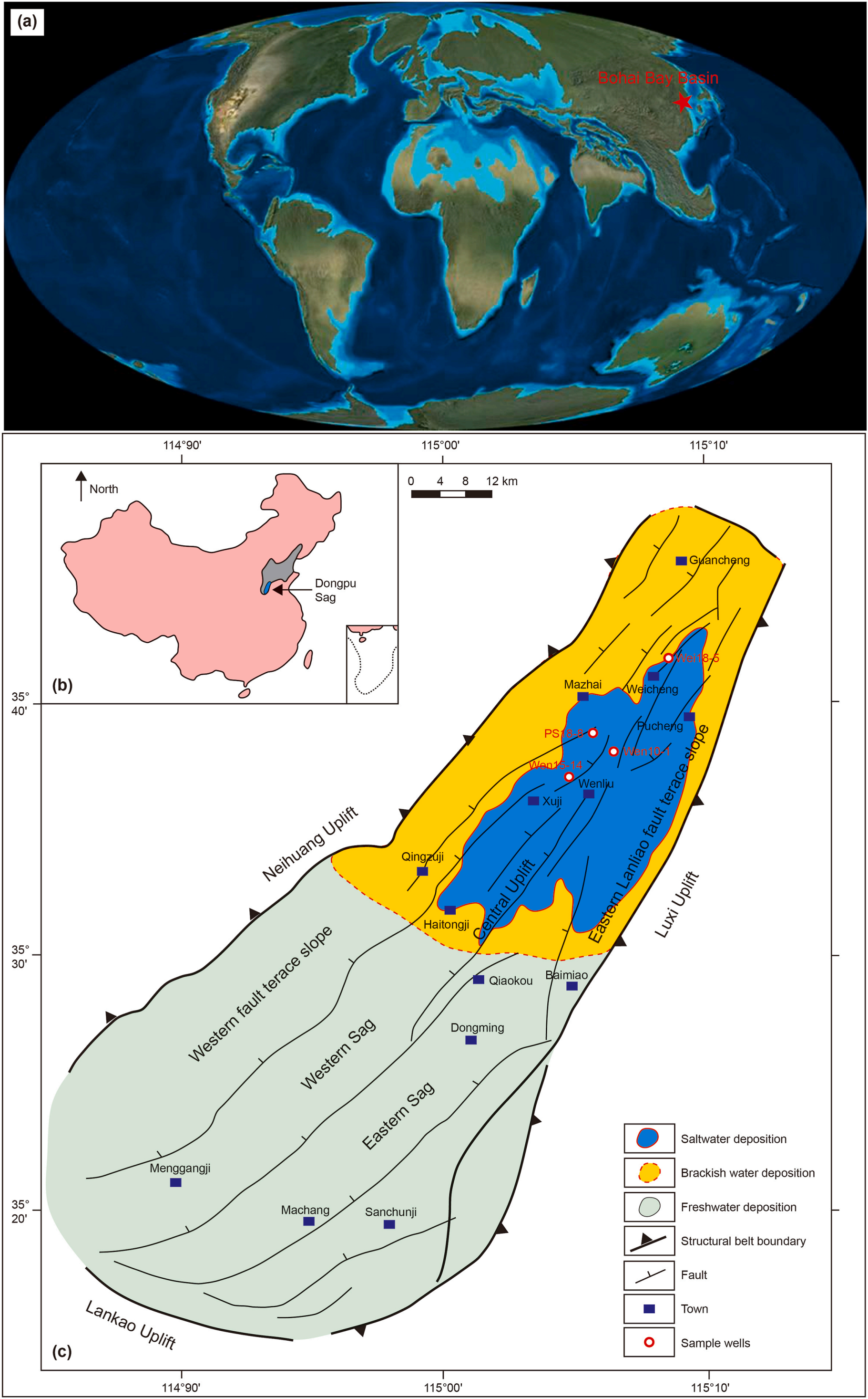
(a)
Bohai Bay Basin
(b)
North
Dongpu Sag
0 4 8 12 km
114°90'
115°00'
115°10'
35° 40'
35° 30'
35° 20'
Guancheng
Wei18-5
Weicheng
Mazhai
Pucheng
PS18-8
Wen10-1
Wen15-14
Wenliu
Xuji
Eastern Lanliao fault terace slope
Neihuang Uplift
Qingzuji
Haitongji
Central Uplift
Luxi Uplift
Qiaokou
Baimiao
Western fault terace slope
Western Sag
Dongming
Eastern Sag
Menggangji
Machang
Sanchunji
Lankao Uplift
(c)
Saltwater deposition
Brackish water deposition
Freshwater deposition
Structural belt boundary
Fault
Town
Sample wells

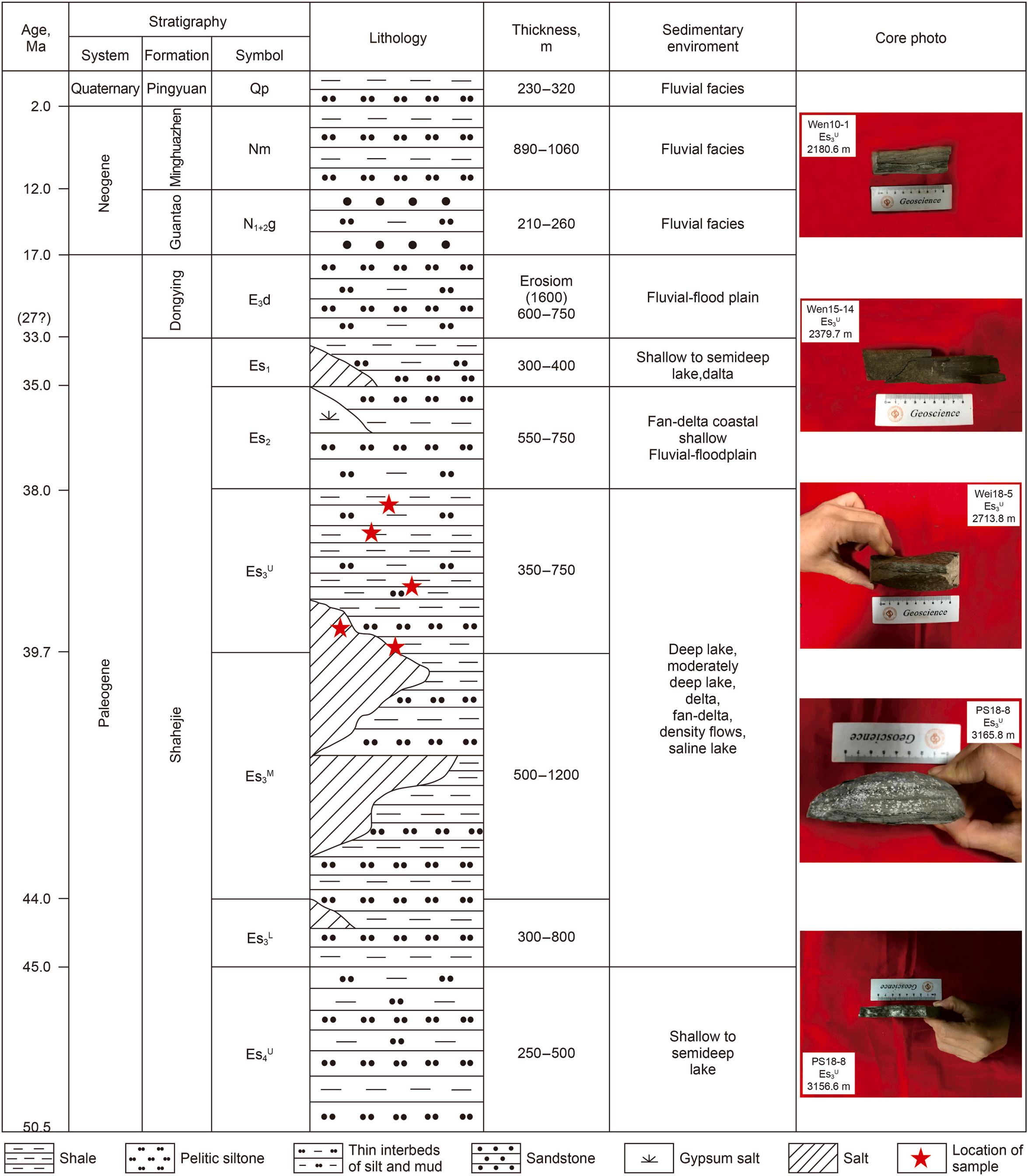
Age, Ma
Stratigraphy
System
Formation
Symbol
Lithology
Thickness, m
Sedimentary enviroment
Core photo
Quaternary
Pingyuan
Qp
230–320
Fluvial facies
2.0
Neogene
Minghuazhen
Nm
890–1060
Fluvial facies
12.0
Guantao
N$_{1+2}$g
210–260
Fluvial facies
17.0
Paleogene
Dongying
E$_3$d
Erosiom (1600) 600–750
Fluvial-flood plain
(27?)
33.0
Shahejie
Es$_1$
300–400
Shallow to semideep lake,dalta
35.0
Es$_2$
550–750
Fan-delta coastal shallow Fluvial-floodplain
38.0
Es$_3^U$
350–750
39.7
Es$_3^M$
500–1200
Deep lake, moderately deep lake, delta, fan-delta, density flows, saline lake
44.0
Es$_3^L$
300–800
45.0
Es$_4^U$
250–500
Shallow to semideep lake
50.5
Wen10-1 Es$_3^U$ 2180.6 m
Wen15-14 Es$_3^U$ 2379.7 m
Wei18-5 Es$_3^U$ 2713.8 m
PS18-8 Es$_3^U$ 3165.8 m
PS18-8 Es$_3^U$ 3156.6 m
Geoscience
Shale
Pelitic siltone
Thin interbeds of silt and mud
Sandstone
Gypsum salt
Salt
Location of sample

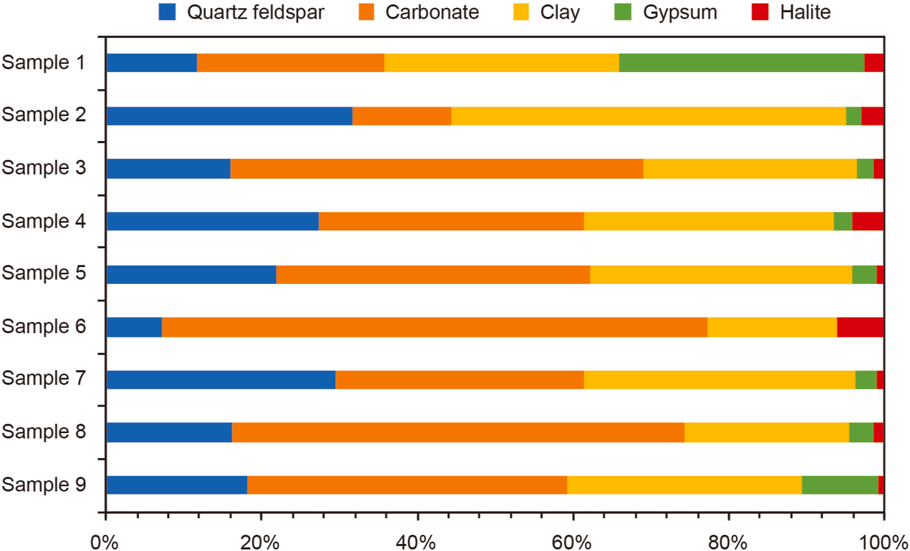
Quartz feldspar
Carbonate
Clay
Gypsum
Halite
Sample 1
Sample 2
Sample 3
Sample 4
Sample 5
Sample 6
Sample 7
Sample 8
Sample 9
0%
20%
40%
60%
80%
100%

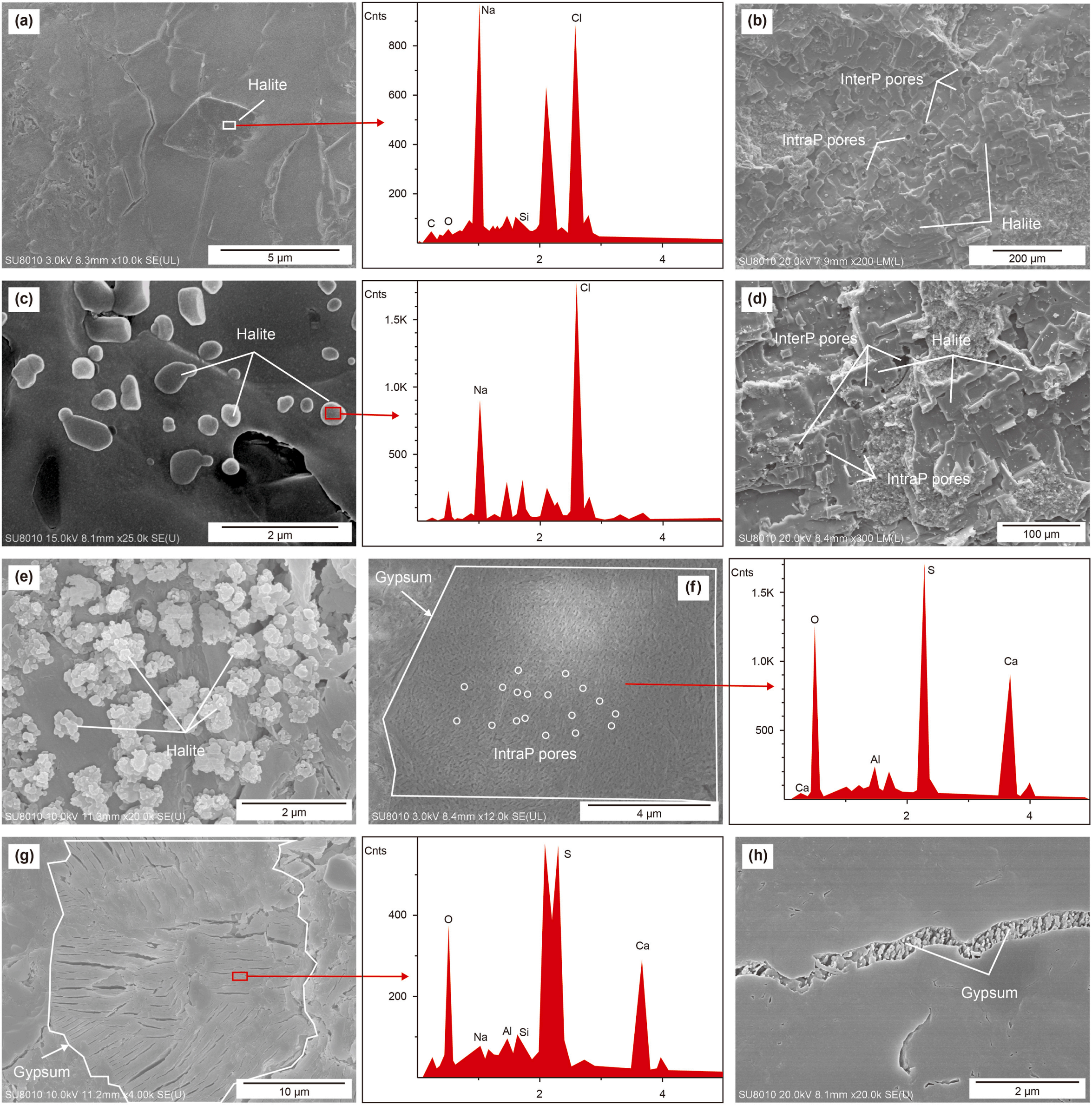
(a)
Halite
SU8010 3.0kV 8.3mm x10.0k SE(UL)
5 µm
Cnts
800
600
400
200
Na
Cl
C
O
Si
2
4
(b)
InterP pores
IntraP pores
Halite
SU8010 20.0kV 7.9mm x200 LM(L)
200 µm
(c)
Halite
SU8010 15.0kV 8.1mm x25.0k SE(U)
2 µm
Cnts
1.5K
1.0K
500
Na
Cl
2
4
(d)
InterP pores
Halite
IntraP pores
SU8010 20.0kV 8.4mm x300 LM(L)
100 µm
(e)
Halite
SU8010 10.0kV 11.3mm x20.0k SE(U)
2 µm
Gypsum
(f)
IntraP pores
SU8010 3.0kV 8.4mm x12.0k SE(UL)
4 µm
Cnts
1.5K
1.0K
500
O
S
Ca
Al
Ca
2
4
(g)
Gypsum
SU8010 10.0kV 11.2mm x4.00k SE(U)
10 µm
Cnts
400
200
O
S
Ca
Na
Al
Si
2
4
(h)
Gypsum
SU8010 20.0kV 8.1mm x20.0k SE(U)
2 µm

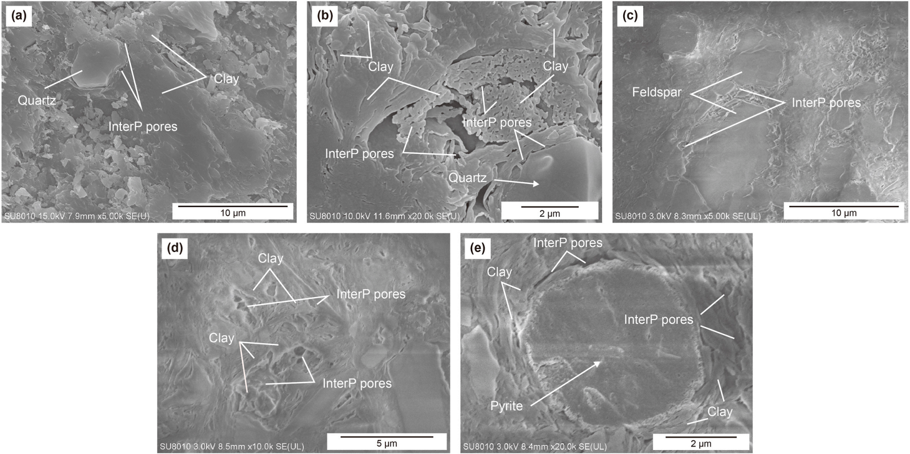
(a)
Quartz
Clay
InterP pores
SU8010 15.0kV 7.9mm x5.00k SE(U)
10 μm
(b)
Clay
Clay
InterP pores
InterP pores
Quartz
SU8010 10.0kV 11.6mm x20.0k SE(U)
2 μm
(c)
Feldspar
InterP pores
SU8010 3.0kV 8.3mm x5.00k SE(UL)
10 μm
(d)
Clay
InterP pores
Clay
InterP pores
SU8010 3.0kV 8.5mm x10.0k SE(UL)
5 μm
(e)
InterP pores
Clay
InterP pores
Pyrite
Clay
SU8010 3.0kV 8.4mm x20.0k SE(UL)
2 μm

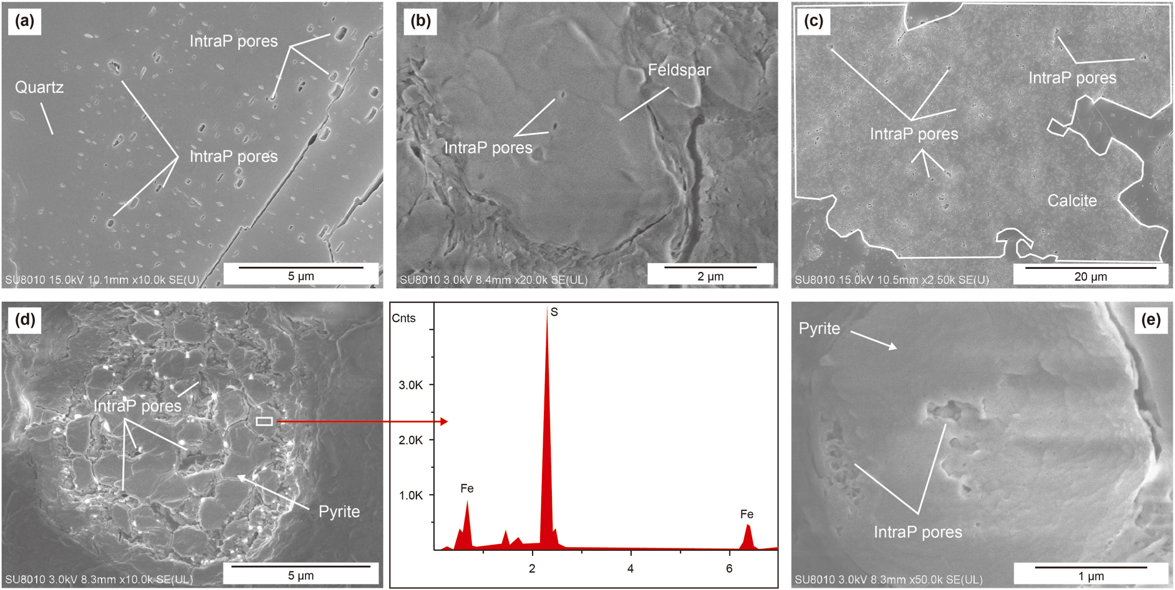
(a)
IntraP pores
Quartz
IntraP pores
5 μm
SU8010 15.0kV 10.1mm x10.0k SE(U)
(b)
Feldspar
IntraP pores
2 μm
SU8010 3.0kV 8.4mm x20.0k SE(UL)
(c)
IntraP pores
IntraP pores
Calcite
20 μm
SU8010 15.0kV 10.5mm x2.50k SE(U)
(d)
IntraP pores
Pyrite
5 μm
SU8010 3.0kV 8.3mm x10.0k SE(UL)
Cnts
S
3.0K
2.0K
1.0K
Fe
Fe
2
4
6
(e)
Pyrite
IntraP pores
1 μm
SU8010 3.0kV 8.3mm x50.0k SE(UL)

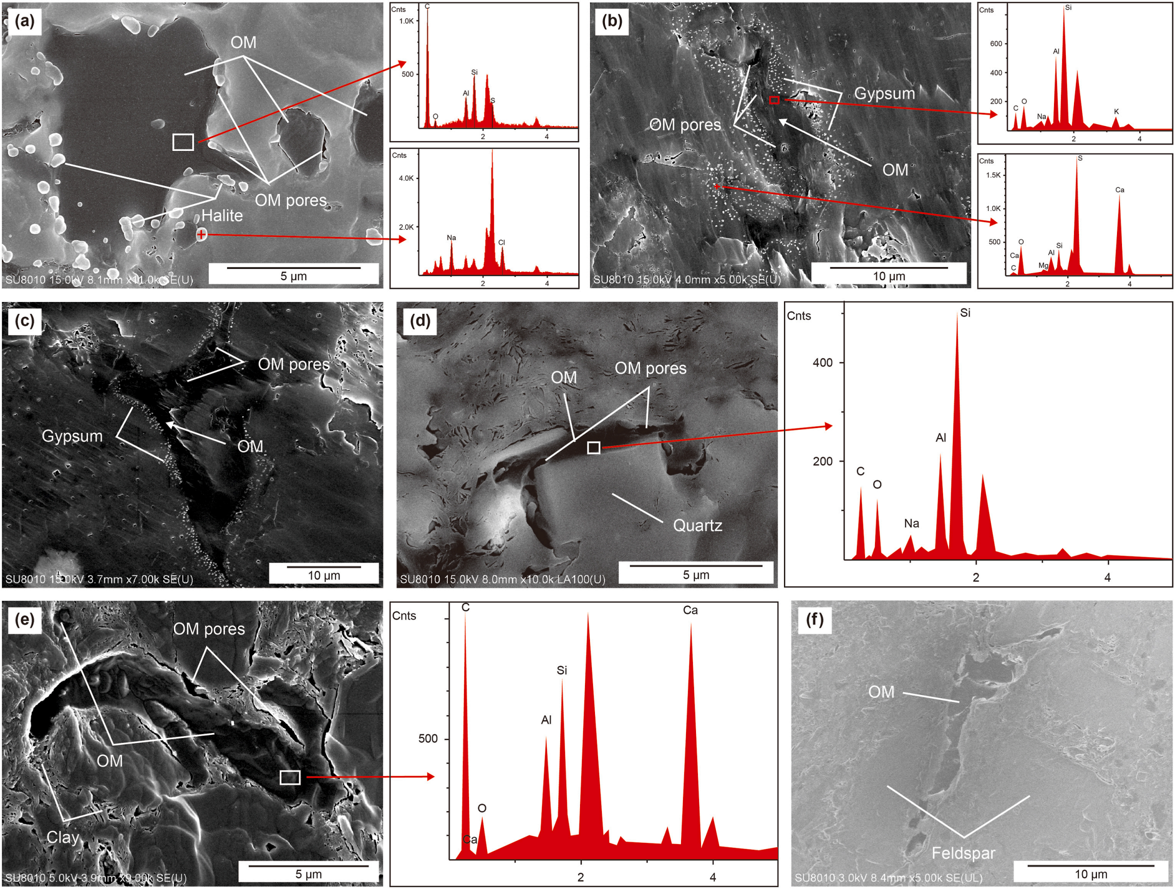
(a)
OM
OM pores
Halite
5 µm
SU8010 15.0kV 8.1mm x11.0k SE(U)
Cnts
1.0K
500
C
O
Al
Si
S
2
4
Cnts
4.0K
2.0K
Na
Cl
2
4
(b)
Gypsum
OM pores
OM
10 µm
SU8010 15.0kV 4.0mm x5.00k SE(U)
Cnts
600
400
200
C
O
Na
Al
Si
K
2
4
Cnts
1.5K
1.0K
500
S
Ca
O
Ca
C
Mg
Al
Si
2
4
(c)
OM pores
Gypsum
OM
10 µm
SU8010 15.0kV 3.7mm x7.00k SE(U)
(d)
OM
OM pores
Quartz
5 µm
SU8010 15.0kV 8.0mm x10.0k LA100(U)
Cnts
400
200
Si
Al
C
O
Na
2
4
(e)
OM pores
OM
Clay
5 µm
SU8010 5.0kV 3.9mm x9.00k SE(U)
Cnts
500
C
Ca
Si
Al
O
Ca
2
4
(f)
OM
Feldspar
10 µm
SU8010 3.0kV 8.4mm x5.00k SE(UL)

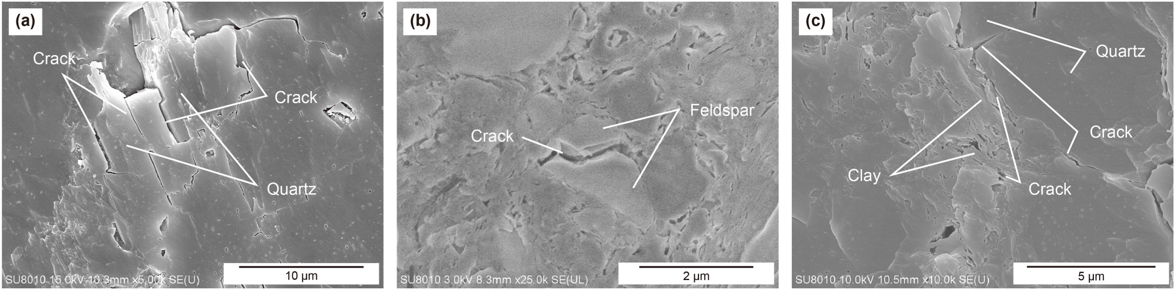
(a)
Crack
Crack
Quartz
SU8010 15.0kV 10.3mm x5.00k SE(U)
10 μm
(b)
Feldspar
Crack
SU8010 3.0kV 8.3mm x25.0k SE(UL)
2 μm
(c)
Quartz
Crack
Clay
Crack
SU8010 10.0kV 10.5mm x10.0k SE(U)
5 μm

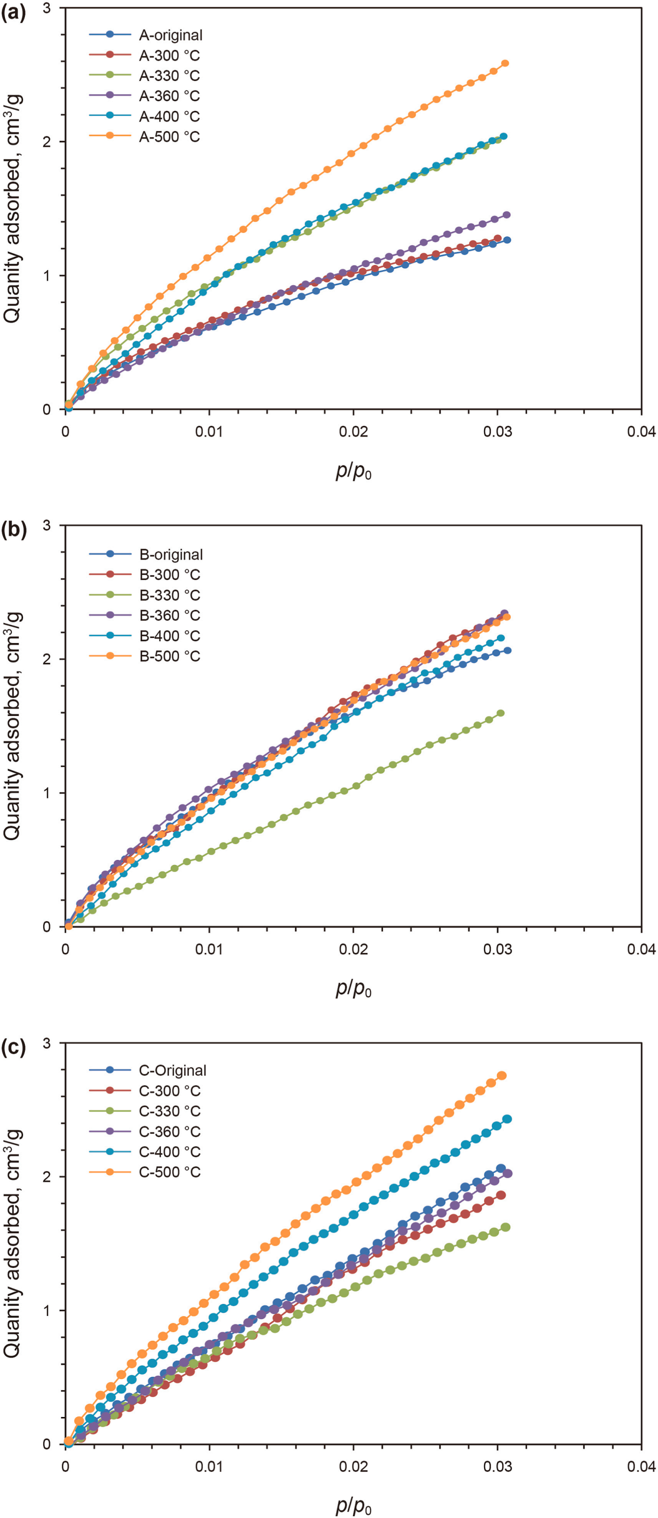
(a)
A-original
A-300 °C
A-330 °C
A-360 °C
A-400 °C
A-500 °C
Quanity adsorbed, cm³/g
0
1
2
3
0
0.01
0.02
0.03
0.04
p/p0
(b)
B-original
B-300 °C
B-330 °C
B-360 °C
B-400 °C
B-500 °C
Quanity adsorbed, cm³/g
0
1
2
3
0
0.01
0.02
0.03
0.04
p/p0
(c)
C-Original
C-300 °C
C-330 °C
C-360 °C
C-400 °C
C-500 °C
Quanity adsorbed, cm³/g
0
1
2
3
0
0.01
0.02
0.03
0.04
p/p0

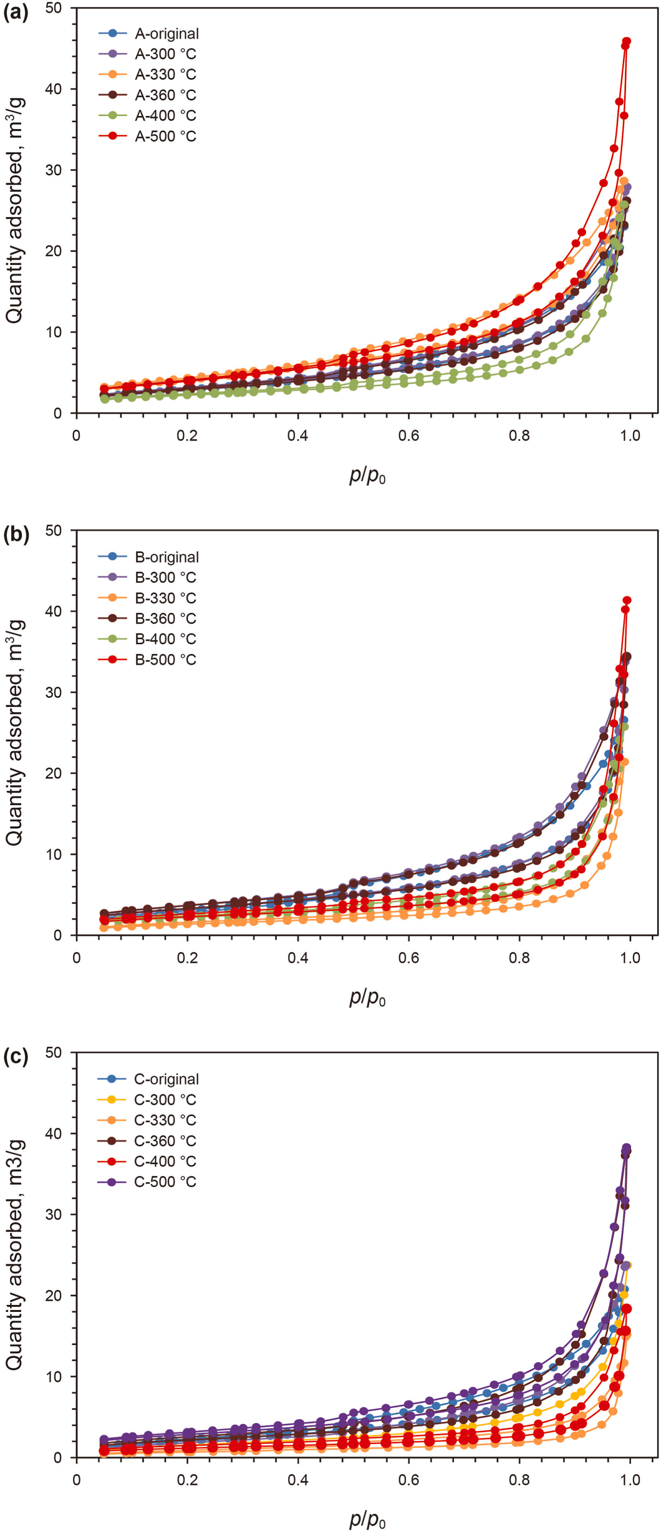
(a)
Quantity adsorbed, m^3/g
p/p_0
A-original
A-300 °C
A-330 °C
A-360 °C
A-400 °C
A-500 °C
0
10
20
30
40
50
0
0.2
0.4
0.6
0.8
1.0
(b)
Quantity adsorbed, m^3/g
p/p_0
B-original
B-300 °C
B-330 °C
B-360 °C
B-400 °C
B-500 °C
0
10
20
30
40
50
0
0.2
0.4
0.6
0.8
1.0
(c)
Quantity adsorbed, m3/g
p/p_0
C-original
C-300 °C
C-330 °C
C-360 °C
C-400 °C
C-500 °C
0
10
20
30
40
50
0
0.2
0.4
0.6
0.8
1.0

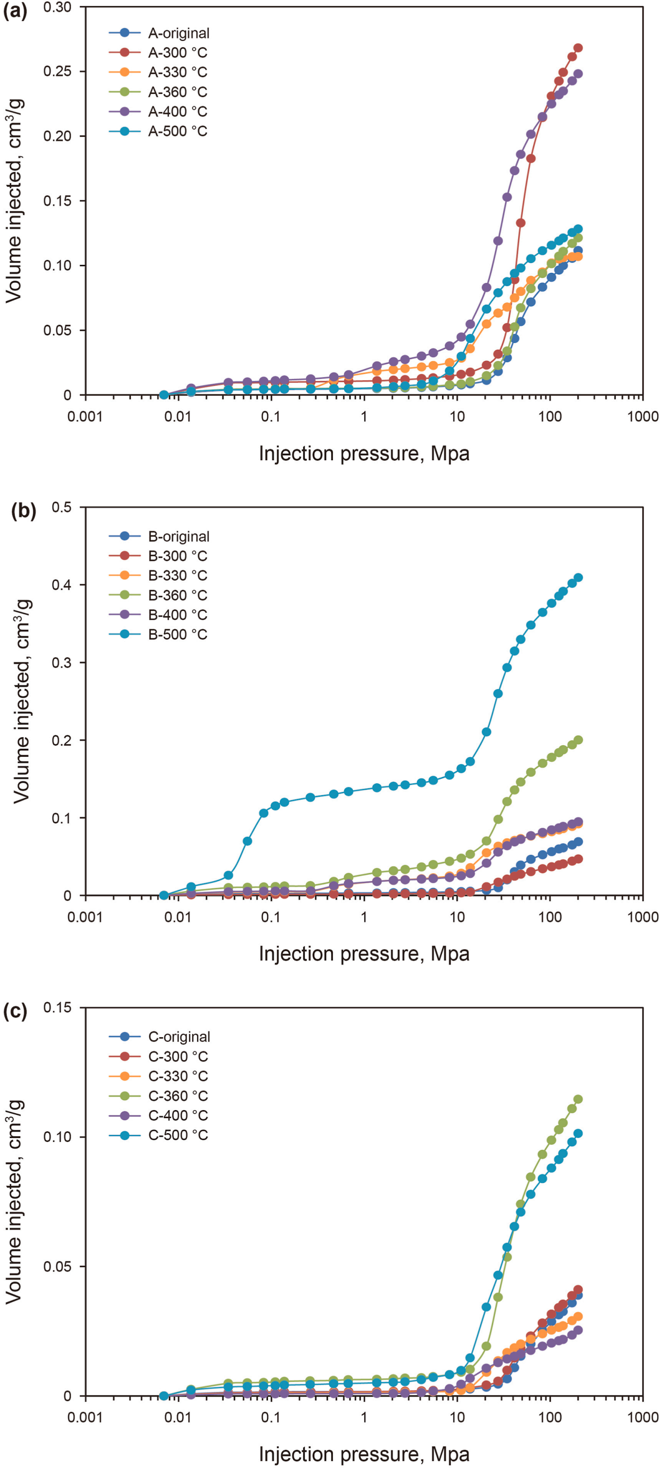
(a)
0.30
0.25
0.20
0.15
0.10
0.05
0
Volume injected, cm^3/g
A-original
A-300 °C
A-330 °C
A-360 °C
A-400 °C
A-500 °C
0.001
0.01
0.1
1
10
100
1000
Injection pressure, Mpa
(b)
0.5
0.4
0.3
0.2
0.1
0
Volume injected, cm^3/g
B-original
B-300 °C
B-330 °C
B-360 °C
B-400 °C
B-500 °C
0.001
0.01
0.1
1
10
100
1000
Injection pressure, Mpa
(c)
0.15
0.10
0.05
0
Volume injected, cm^3/g
C-original
C-300 °C
C-330 °C
C-360 °C
C-400 °C
C-500 °C
0.001
0.01
0.1
1
10
100
1000
Injection pressure, Mpa

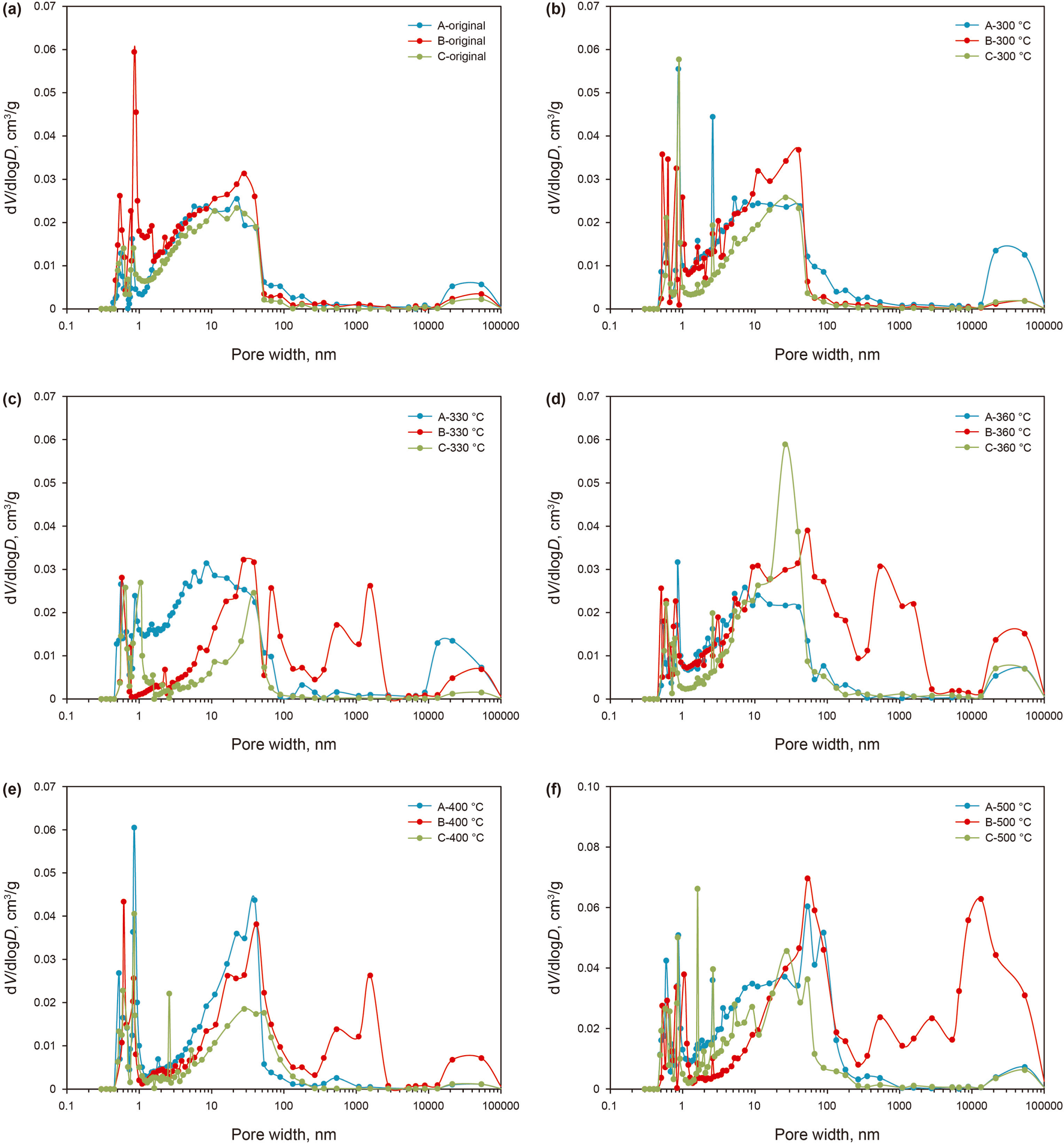
(a)
A-original
B-original
C-original
(b)
A-300 °C
B-300 °C
C-300 °C
(c)
A-330 °C
B-330 °C
C-330 °C
(d)
A-360 °C
B-360 °C
C-360 °C
(e)
A-400 °C
B-400 °C
C-400 °C
(f)
A-500 °C
B-500 °C
C-500 °C
dV/dlogD, cm³/g
Pore width, nm
0
0.01
0.02
0.03
0.04
0.05
0.06
0.07
0.08
0.10
0.1
1
10
100
1000
10000
100000

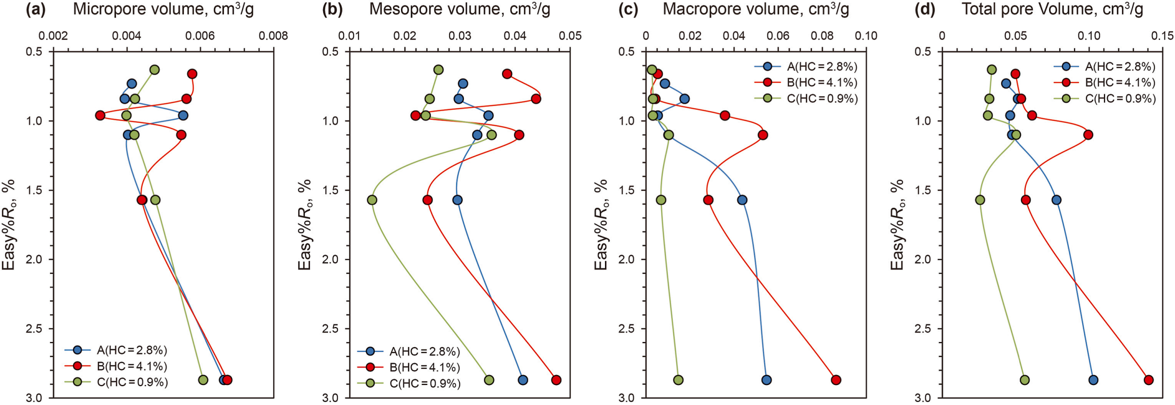
(a) Micropore volume, cm³/g
0.002
0.004
0.006
0.008
(b) Mesopore volume, cm³/g
0.01
0.02
0.03
0.04
0.05
(c) Macropore volume, cm³/g
0
0.02
0.04
0.06
0.08
0.10
(d) Total pore Volume, cm³/g
0
0.05
0.10
0.15
Easy%Ro, %
0.5
1.0
1.5
2.0
2.5
3.0
A(HC = 2.8%)
B(HC = 4.1%)
C(HC = 0.9%)

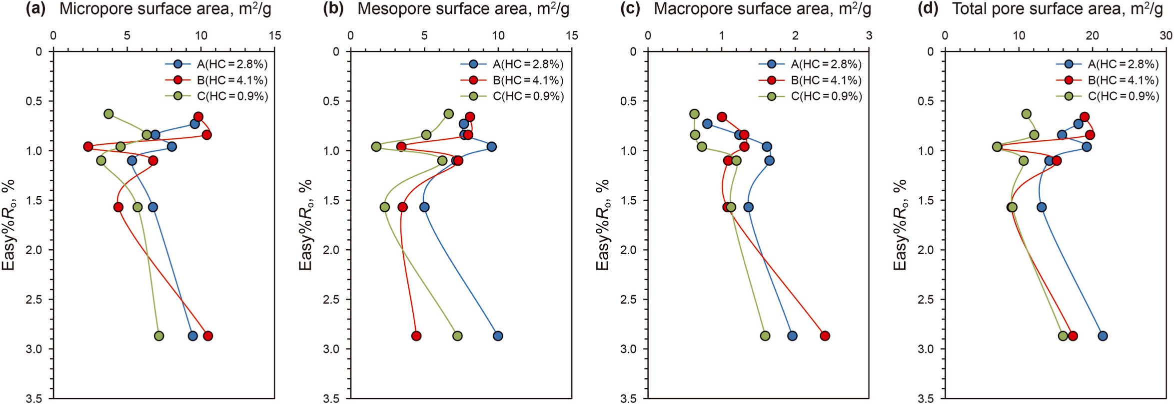
(a) Micropore surface area, m²/g
(b) Mesopore surface area, m²/g
(c) Macropore surface area, m²/g
(d) Total pore surface area, m²/g
0
5
10
15
0
1
2
3
0
10
20
30
Easy%Ro, %
0
0.5
1.0
1.5
2.0
2.5
3.0
3.5
A(HC = 2.8%)
B(HC = 4.1%)
C(HC = 0.9%)

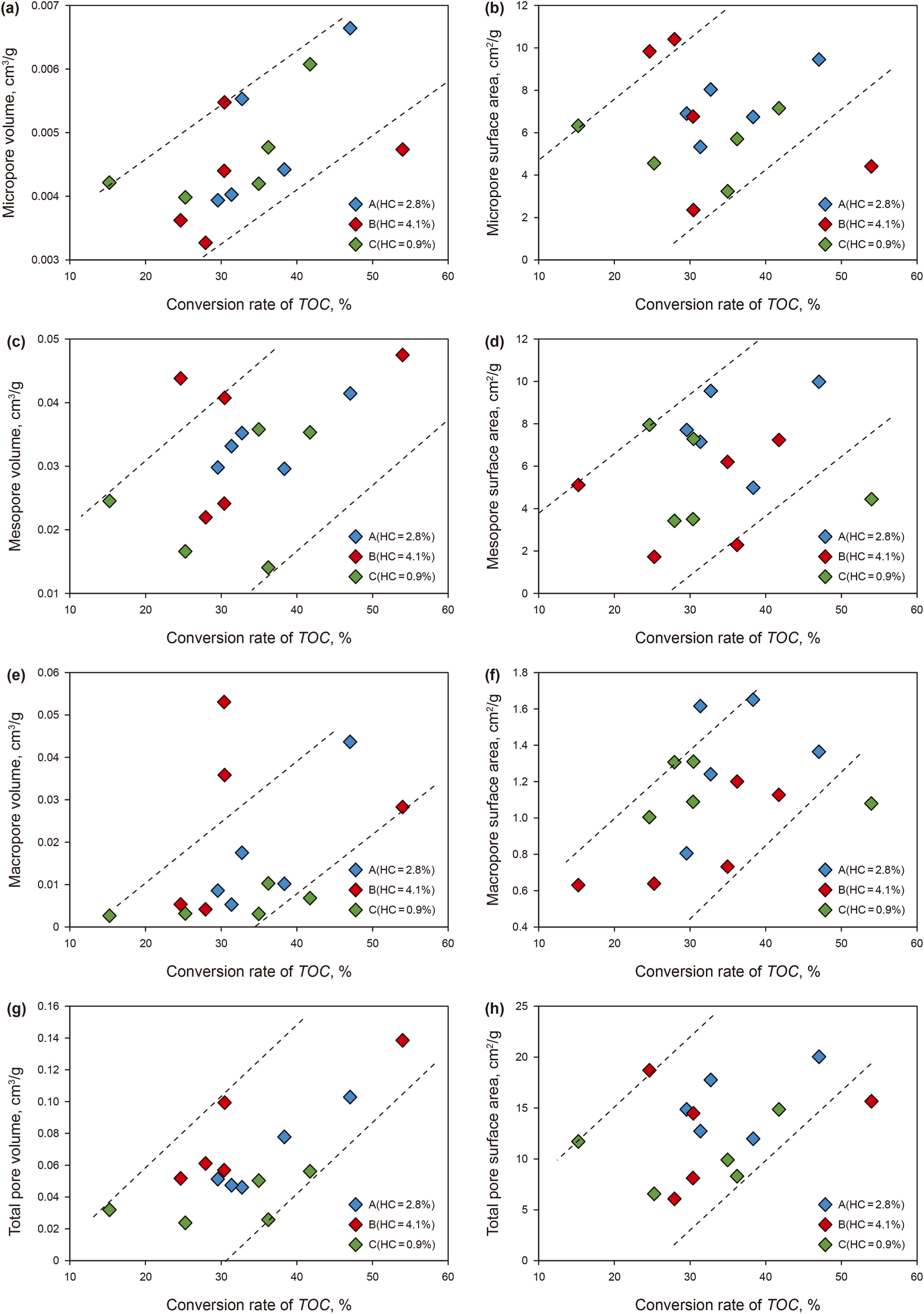
(a)
Micropore volume, cm^3/g
0.003
0.004
0.005
0.006
0.007
Conversion rate of *TOC*, %
10
20
30
40
50
60
A(HC = 2.8%)
B(HC = 4.1%)
C(HC = 0.9%)
(b)
Micropore surface area, cm^2/g
0
2
4
6
8
10
12
Conversion rate of *TOC*, %
A(HC = 2.8%)
B(HC = 4.1%)
C(HC = 0.9%)
(c)
Mesopore volume, cm^3/g
0.01
0.02
0.03
0.04
0.05
Conversion rate of *TOC*, %
A(HC = 2.8%)
B(HC = 4.1%)
C(HC = 0.9%)
(d)
Mesopore surface area, cm^2/g
0
2
4
6
8
10
12
Conversion rate of *TOC*, %
A(HC = 2.8%)
B(HC = 4.1%)
C(HC = 0.9%)
(e)
Macropore volume, cm^3/g
0
0.01
0.02
0.03
0.04
0.05
0.06
Conversion rate of *TOC*, %
A(HC = 2.8%)
B(HC = 4.1%)
C(HC = 0.9%)
(f)
Macropore surface area, cm^2/g
0.4
0.6
0.8
1.0
1.2
1.4
1.6
1.8
Conversion rate of *TOC*, %
A(HC = 2.8%)
B(HC = 4.1%)
C(HC = 0.9%)
(g)
Total pore volume, cm^3/g
0
0.02
0.04
0.06
0.08
0.10
0.12
0.14
0.16
Conversion rate of *TOC*, %
A(HC = 2.8%)
B(HC = 4.1%)
C(HC = 0.9%)
(h)
Total pore surface area, cm^2/g
0
5
10
15
20
25
Conversion rate of *TOC*, %
A(HC = 2.8%)
B(HC = 4.1%)
C(HC = 0.9%)

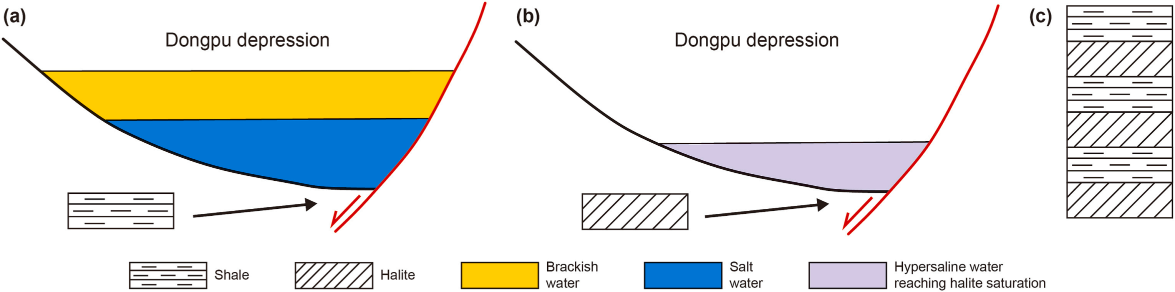
(a)
Dongpu depression
(b)
Dongpu depression
(c)
Shale
Halite
Brackish water
Salt water
Hypersaline water reaching halite saturation

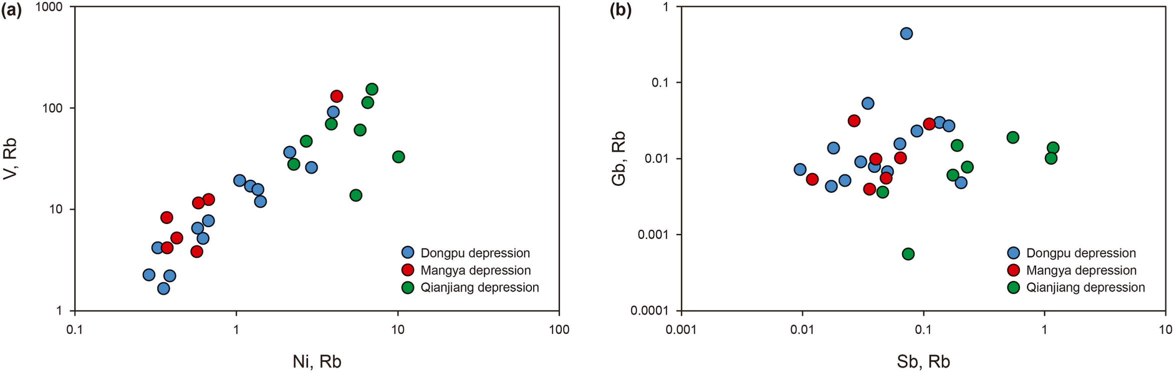
(a)
1000
100
10
1
V, Rb
0.1
1
10
100
Ni, Rb
Dongpu depression
Mangya depression
Qianjiang depression
(b)
1
0.1
0.01
0.001
0.0001
Gb, Rb
0.001
0.01
0.1
1
10
Sb, Rb
Dongpu depression
Mangya depression
Qianjiang depression

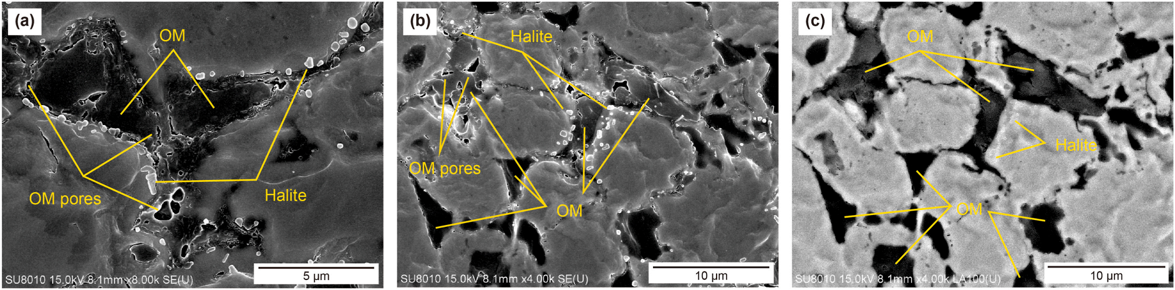
(a)
OM
OM pores
Halite
5 μm
SU8010 15.0kV 8.1mm x8.00k SE(U)
(b)
Halite
OM pores
OM
10 μm
SU8010 15.0kV 8.1mm x4.00k SE(U)
(c)
OM
Halite
OM
10 μm
SU8010 15.0kV 8.1mm x4.00k LA100(U)

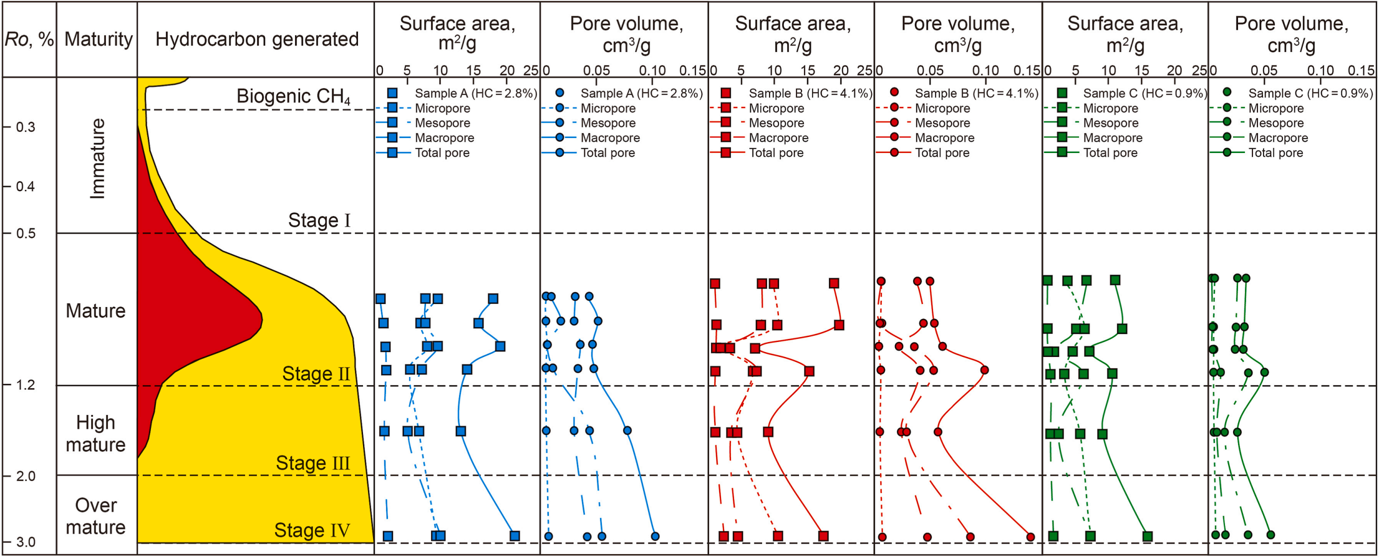
Ro, %
Maturity
Hydrocarbon generated
Surface area, m^2/g
Pore volume, cm^3/g
Surface area, m^2/g
Pore volume, cm^3/g
Surface area, m^2/g
Pore volume, cm^3/g
0 5 10 15 20 25
0 0.05 0.10 0.15
0.3
0.4
0.5
1.2
2.0
3.0
Immature
Mature
High mature
Over mature
Biogenic CH$_4$
Stage I
Stage II
Stage III
Stage IV
Sample A (HC = 2.8%)
Sample B (HC = 4.1%)
Sample C (HC = 0.9%)
Micropore
Mesopore
Macropore
Total pore

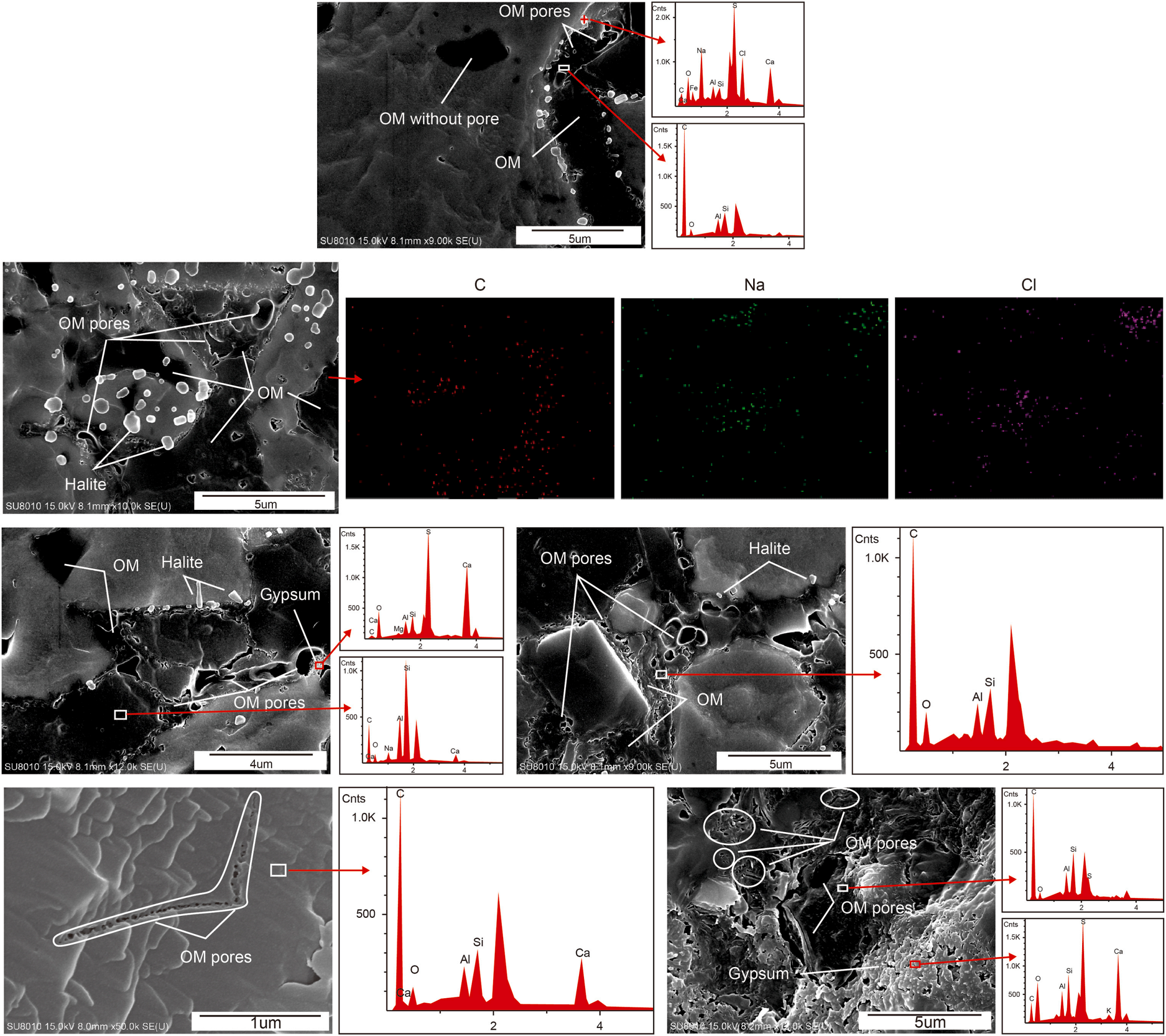
OM pores
OM without pore
OM
SU8010 15.0kV 8.1mm x9.00k SE(U)
5um
Cnts
2.0K
1.0K
S
Na
Cl
Ca
O
Fe
C
Ca
Al
Si
2
4
Cnts
1.5K
1.0K
500
C
O
Al
Si
2
4
OM pores
OM
Halite
SU8010 15.0kV 8.1mm x10.0k SE(U)
5um
C
Na
Cl
OM
Halite
Gypsum
OM pores
SU8010 15.0kV 8.1mm x12.0k SE(U)
4um
Cnts
1.5K
1.0K
500
S
Ca
O
Ca
C
Mg
Al
Si
2
4
Cnts
1.0K
500
Si
C
O
Ca
Na
Al
Ca
2
4
OM pores
Halite
OM
SU8010 15.0kV 8.1mm x9.00k SE(U)
5um
Cnts
1.0K
500
C
O
Al
Si
2
4
OM pores
SU8010 15.0kV 8.0mm x50.0k SE(U)
1um
Cnts
1.0K
500
C
O
Ca
Al
Si
Ca
2
4
OM pores
OM pores
Gypsum
SU8010 15.0kV 8.2mm x12.0k SE(U)
5um
Cnts
1.0K
500
C
O
Al
Si
S
2
4
Cnts
1.5K
1.0K
500
S
Ca
C
O
Al
Si
K
2
4

Declaration of interests

☒ The authors declare that they have no known competing financial interests or personal relationships that could have appeared to influence the work reported in this paper.

☐ The authors declare the following financial interests/personal relationships which may be considered as potential competing interests: